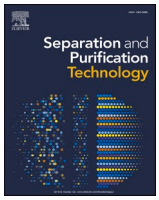
Separation and Purification Technology 426 (2027) 140937



Contents lists available at ScienceDirect

Separation and Purification Technology

journal homepage: www.elsevier.com/locate/seppur



Cellulose nanofiber-reinforced MXene–κ-carrageenan membrane for simultaneous removal of PFAS and co-contaminants from groundwater: Chain length-dependent performance

Rokhsare Kardani [a], Brett Turner [a], Zhaohua He [a], Viktoria Mueller [b,d], Andreas Roth [b], Syed Javaid Zaidi [c], I.M.R. Fattah [a], Ali Altaee [a,*]

[a] Centre for Green Technology, School of Civil, Environmental & Sociotechnical Engineering, University of Technology Sydney, 15 Broadway, NSW, 2007, Australia
[b] Institute of Chemistry, University of Graz, Universitätsplatz 1, A-8010 Graz, Austria
[c] Center of Advanced Materials, Qatar University, PO, Box 2713, Doha, Qatar
[d] The James Hutton Institute, Craigiebuckler, Aberdeen AB15 8QH, United Kingdom

ARTICLE INFO

Editor name: Junyong Zhu

Keywords:
PFAS removal
Filtration
Hydrogel membranes
MXene
Kappa-carrageenan

ABSTRACT

Per- and polyfluoroalkyl substances (PFAS) are persistent groundwater contaminants whose structural diversity, particularly the presence of short- and ultra-short-chain compounds, presents significant challenges for membrane-based separation. In this study, a biopolymer-based nanocomposite hydrogel membrane incorporating κ-carrageenan (κC), cellulose nanofibers (CNF), polyethyleneimine (PEI), and MXene nanosheets was developed for the simultaneous removal of PFAS and trace metals from contaminated groundwater. The incorporation of MXene improved membrane transport and separation performance, with an optimal loading of 0.05 wt% (κC-MX.05). At an operating pressure of 3 bar, the optimised membrane achieved water fluxes of 9.31 and 7.97 L/m^{2}h, with rejection rates of 86.45% and 95.65% for NaCl and $MgSO_4$, respectively. When evaluated using real PFAS-contaminated groundwater, the membrane showed a water flux of 6.8 L/m^{2}h and demonstrated effective removal of PFAS across different chain lengths, including 88.2% rejection of ultra-short-chain trifluoroacetic acid (TFA) and 98.9% rejection of PFOA. The dominant regulated PFAS, PFHxS and PFOS, exhibited rejection rates above 96.92% and 99.32%, respectively, over three filtration cycles. Simultaneously, trace metals, including Zn, Al, and Mn, were removed with rejection rates of 98–≈100%. The membrane also achieved a flux recovery ratio of 88.99%, indicating favorable antifouling performance. These findings demonstrate the potential of MXene-enhanced biopolymer hydrogel membranes for low-pressure treatment of groundwater containing PFAS of varying chain lengths and co-occurring metal contaminants.

1. Introduction

Per- and polyfluoroalkyl substances (PFAS) are a large group of highly fluorinated synthetic compounds known for their exceptional environmental persistence and resistance to water and oils. Because of these unique features, they have been widely used in industrial and commercial applications such as firefighting foams, textile treatment, paper and leather coatings, and corrosion protection. PFAS are also concerning due to their bioaccumulation potential and affinity for proteins in biological tissues. As a result of their extensive use and persistence, they are now widely detected in air, soil, water, and living organisms [1]. Legacy landfill sites are important sources of PFAS contamination in groundwater, where persistent compounds such as PFOS, PFOA, and PFHxS can remain for decades and threaten drinking water quality and aquatic ecosystems [2].

PFAS comprise a broad and chemically diverse group of fluorinated substances with varying physical and chemical properties. They are generally classified into polymeric and non-polymeric forms. Polymeric PFAS, e.g., fluoropolymers and fluorinated side-chain polymers, are widely used in industrial products and act as precursors of smaller and more hazardous PFAS through environmental degradation. In water treatment, non-polymeric PFAS are of greater concern and mainly include perfluoroalkyl and polyfluoroalkyl acids, with the latter often transforming into the more persistent perfluoroalkyl acids in the

* Correspondent author..
E-mail address: ali.altaee@uts.edu.au (A. Altaee).

https://doi.org/10.1016/j.seppur.2026.140937
Received 15 September 2026; Received in revised form 14 October 2026; Accepted 11 November 2026
Available online 12 November 2026
1383-5866/© 2026 The Author(s). Published by Elsevier B.V. This is an open access article under the CC BY license (http://creativecommons.org/licenses/by/4.0/).

environment. Among these, perfluoroalkyl carboxylic acids and perfluoroalkyl sulfonic acids are the most studied due to their persistence, toxicity, widespread occurrence, and resistance to biodegradation. PFAS are also commonly classified as long- and short-chain compounds, depending on the number of carbon atoms, with chain length strongly influencing their environmental behaviour and removal performance. In addition, emerging alternatives like ether-based PFAS are increasingly detected in water sources, although many of their properties, environmental fate, and treatment behaviour remain inadequately understood [3].

Conventional treatment methods, such as coagulation, sedimentation, conventional filtration, and oxidation, are generally ineffective for PFAS removal due to the stability of their chemical structure, surfactant nature that keeps them soluble, and oleophobic nature. Therefore, advanced methods such as adsorption, ion exchange, and membrane filtration are commonly used. Adsorption and ion exchange can be effective, but both face challenges related to regeneration, cost, and reduced performance for some PFAS species. Among membrane processes, MF and UF are usually less effective due to their large molecular weight cut-off, whereas Nanofiltration (NF) and reverse osmosis (RO) achieve much higher PFAS rejection through size exclusion, electrostatic interactions, and solution-diffusion [4].

Several studies reported an exceptional PFAS rejection ranging from 90% to 99% for a wide range of PFAS compounds by NF and RO membranes. However, these systems are typically based on commercially available membranes that require high operating pressures, significant energy input, and experience water flux degradation due to fouling [4,5]. In addition, their performance is often evaluated using simplified feed solutions, whereas PFAS-contaminated groundwater and wastewater are complex mixtures of organic matter, coexisting ions, and competing species that can influence separation behaviour [6–8]. Furthermore, membrane rejection is often more variable for short-chain and ultrashort-chain PFAS, highlighting ongoing challenges in achieving consistent removal under realistic conditions [9].

To address the limitations of NF and RO membranes, scientists developed nanoparticle-based membranes with distinct features for PFAS treatment. For example, Zhi et al. [9] developed layer-by-layer nanofiltration membranes for PFAS removal and found that the $(PDADMAC/PSS)_3$ membrane achieved the best performance, with 86.1–98.1% rejection of short-chain PFAS and more than 99.9% removal of long-chain PFAS. The study also showed that increasing feed pH from 3.5 to 9.0 raised average PFAS rejection by 16.6% to 32.0%, while testing with real sewage effluent gave removal efficiencies of 82.5% for PFOA and 96.7% for PFOS. Safulko et al. [10] evaluated four high-pressure membranes, ranging from loose NF to seawater RO, for the removal of nine perfluoroalkyl acids in a pilot-scale closed-circuit membrane filtration system operated up to 97% water recovery. They found that the tight NF90, CR100, and SW30 membranes achieved overall rejection values above 98.3%, whereas the loose NF270 membrane showed the lowest rejection, particularly at water recoveries greater than 90%. Aedan et al. [8] investigated the PSRNF TS80 membrane for PFAS removal from contaminated groundwater under different pH and pressure conditions. The membrane achieved high rejection of long-chain PFAS, including PFOS, PFDA, PFNA, and PFOA (99.3–100%), while short-chain PFAS such as PFHxS, PFHpA, and PFHxA were rejected by 96.9–99.1%. Ultra-short-chain PFAS showed lower but still notable rejection, reaching 91–92.6% for TFA, TFMS, PFPrA, and PFPrS under optimised conditions. The improved removal was mainly attributed to steric hindrance and electrostatic repulsion, with alkaline pH enhancing ultra-short-chain PFAS rejection. Ma et al. [11] fabricated an MXene-modified polyamide nanofiltration membrane for short-chain PFAS removal and reported that water permeability increased from 8.65 to 12.16 L/m^2hbar^{-1} after MXene incorporation. The modified membrane also achieved high rejection of PFHxS and PFHxA, reaching 96.85% and 93.35%, respectively, due to the improved membrane hydrophilicity, greater negative surface charge, and stronger electrostatic and hydrogen-bonding interactions with PFAS. Generally, there are attempts to replace polyamide-based membranes with natural polymers of lower environmental pollution and contribution to greenhouse gas emissions. Natural polymers were successfully used in water and wastewater treatment, with high permselectivity and antifouling characteristics [12].

To address these issues, this study investigated the design and development of a κ-carrageenan (κC)-based composite hydrogel membrane incorporating cellulose nanofibers (CNF), polyethyleneimine (PEI), and MXene nanosheets for the treatment of PFAS-contaminated groundwater. The novelty of this study lies in combining MXene and CNF into a biodegradable κ-carrageenan/PEI hydrogel membrane to achieve broad-spectrum PFAS rejection, including ultra-short-chain PFAS, under real groundwater conditions, while simultaneously evaluating co-contaminant removal and antifouling performance. κC was selected due to its biodegradability, environmental compatibility, abundance of sulfate and hydroxyl functional groups, and tunable mechanical properties through crosslinking, making it a promising material for sustainable water treatment. PEI crosslinking introduces amine groups ($-NH_2$), improving the structural stability of the backbone κC hydrogel and the electrostatic attraction of anionic PFAS compounds, while reducing membrane swelling that could weaken adhesion to the support layer [13–15]. CNF was incorporated to improve the membrane structural integrity, membrane porosity, and hydrophilicity, resisting the adhesion of fouling materials to maintain the desirable water flux over time. MXene nanosheets were introduced to improve hydrophilicity, separation performance, and potential antifouling properties [16,17]. The research questions are: i) what is the impact of MXene loading on the membrane permeability and selectivity? ii) what is the membrane selectivity and rejection for long-, short-, and ultrashort-chain PFAS compounds? And iii) what are the performance and antifouling characteristics of the developed membrane in multiple filtration cycles? The membrane was proposed as a low-pressure and environmentally friendly alternative with relatively simple fabrication, and the effect of MXene loading on membrane structure and performance was systematically investigated. Structural and physicochemical analyses were conducted to characterize the fabricated membranes. Water uptake, swelling degree, porosity, pore size, water contact angle, zeta potential, and mechanical strength were measured for all membranes. In addition, membrane performance was assessed through pure water flux, NaCl and $MgSO_4$ rejection, and treatment of PFAS-contaminated groundwater to evaluate the simultaneous removal of PFAS, heavy metals, and organic matter under realistic conditions.

Table 1
Groundwater characteristics and composition.

Parameter	Value
Appearance	Colorless and clear
Total suspended solids	2 ± 0.5 mg/L
Total dissolved solid	123.1 ± 5 mg/L
Total organic carbon	42.7 ± 2 mg/L
Conductivity	130.5 ± 5 μs/cm
Salinity	117 ± 5 mg/L
Turbidity	1.6 ± 0.2 NTU
pH	5.8 ± 0.2
Na	13.73 ± 2 mg/L
Mg	38.77 ± 2 mg/L
Ca	65.23 ± 2 mg/L
Zn	12.76 ± 2 mg/L
Al	0.24 ± 0.2 mg/L
Mn	0.15 ± 0.1 mg/L

Table 2
PFAS profile, chain length, and concentration levels in groundwater.

Class	PFAS compound	Abbreviation	Chain length And classification	Concentration (ng/L)
Perfluoroalkyl carboxylic acids (PFCA)	Trifluoroacetic acid	TFA	C2 **Ultrashort-chain**	11,000
	Perfluorobutanoic acid	PFBA	C4 **Short-chain**	3426
	Perfluoropentanoic acid	PFPeA	C5 **Short-chain**	3588
	Perfluorohexanoic acid	PFHxA	C6 **Short-chain**	19,632
	Perfluoroheptanoic acid	PFHpA	C7 **Short-chain**	4560
	Perfluorooctanoic acid	PFOA	C8 **Long-chain**	11,218
Perfluoroalkyl sulfonic acids (PFSA)	Perfluorobutane sulfonate	PFBS	C4 **Short-chain**	6800
	Perfluoropentane sulfonate	PFPeS	C5 **Short-chain**	5608
	Perfluorohexane sulfonate	PFHxS	C6 **Long-chain**	32,000
	Perfluorooctane sulfonate	PFOS	C8 **Long-chain**	34,000
Other / emerging PFAS	Perfluorobutane sulfonamide	FBSA	C4 **Short-chain**	2416
	Perfluorohexane sulfonamide	FHxSA	C6 **Long-chain**	3262
	8:2 fluorotelomer phosphate diester	8:2 diPAP	C8 fluorotelomer diester[a] **Long-chain**	1500

[a] 8:2 diPAP is a phosphate diester containing two fluorotelomer chains; therefore, its chain length is not directly comparable to single-chain PFCAs/PFSAs.

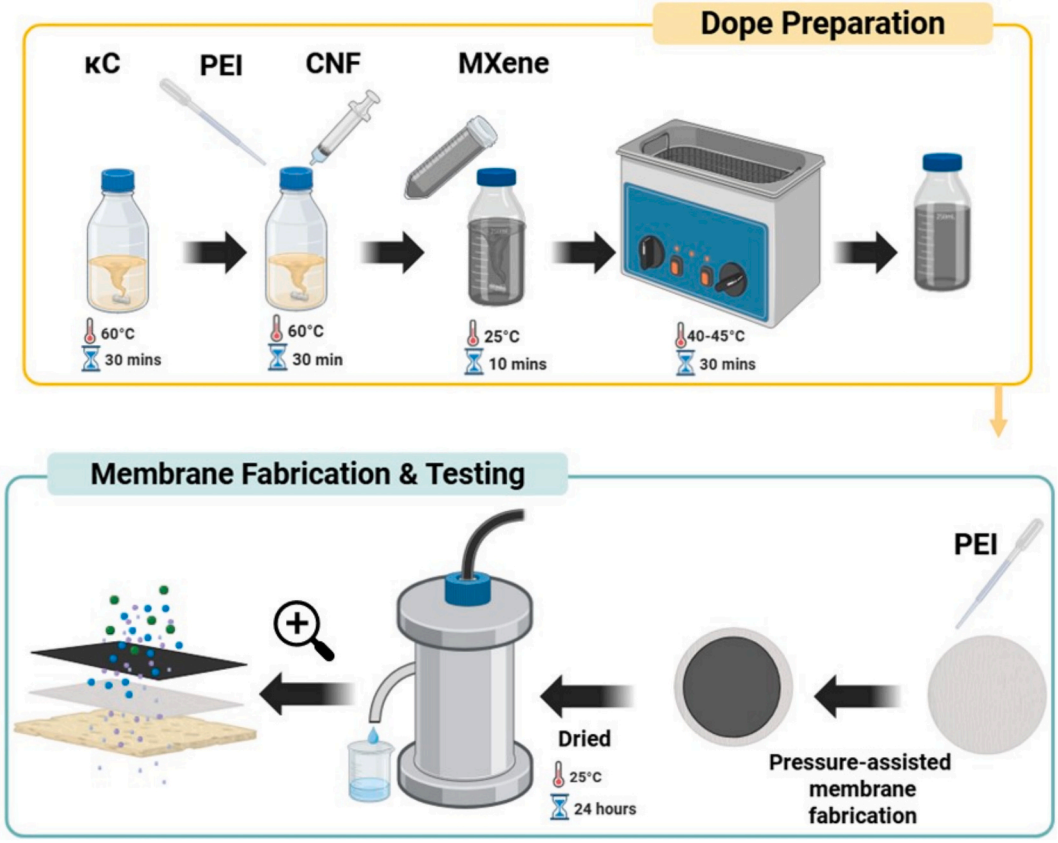


Fig. 1. Schematic illustration of the preparation of the κC-CNF/PEI-MXene hydrogel membranes, including dope solution preparation, pressure-assisted membrane fabrication, drying, and subsequent filtration testing.

2. Experimental Section

2.1. Materials

All chemicals used in this study were of analytical grade and applied as received without further purification. κ-carrageenan (κC), a sulfated plant polysaccharide, and branched polyethyleneimine (PEI) with an average molecular weight of 25,000 g/mol were purchased from Sigma-Aldrich (Australia). Cellulose nanofibers (CNF) were obtained from Nanography. Titanium carbide MXene (Ti_3C_2, multilayer powder, Sigma-Aldrich) was used as the MXene nanofiller in this study.

PFAS-contaminated groundwater was collected from a highly impacted monitoring well within the Williamtown PFAS Management Area associated with RAAF Base Williamtown, New South Wales, Australia. The site has been affected by historical use of PFAS-containing aqueous film-forming foams (AFFF), and Defence investigations identified multiple on-base PFAS source areas and groundwater/surface-water migration pathways [18]. The groundwater was stored at 4 °C to minimize changes in composition. The main characteristics of the groundwater are presented in Table 1, and the concentrations of detected PFAS are provided in Table 2. Sodium chloride (NaCl) and magnesium sulfate ($MgSO_4$) purchased from Sigma-Aldrich (Australia) were used to prepare model salt solutions for membrane performance and permselectivity evaluation. Deionized (DI) water was used for membrane and dope solution preparation in all experimental procedures.

A hydrophilic cellulose acetate (CA) membrane filter paper (Thermo Fisher Scientific, Sartorius Stedim Biotech GmbH, Germany) with a pore size of 0.2 μm, diameter of 47 mm, and thickness of 120 μm was used as the support layer for membrane fabrication. The CA support was selected due to its good mechanical strength, chemical stability, and hydrophilicity, which facilitate effective interaction with the hydrogel layer and support water permeation during filtration.

2.2. Membrane fabrication

A 3% (wt/*v*) κ-carrageenan (κC) solution was prepared by dissolving the polymer powder in deionized (DI) water at 60 °C under continuous stirring for 3 h until a homogeneous gel-like solution was obtained. The solution was allowed to cool to room temperature until a slightly gel-like consistency developed, after which it was homogenized at 450 rpm for 1 h using a top blender to ensure better uniformity (Fig. 1).

A 2.5% (wt/*v*) cellulose nanofiber (CNF) dispersion was prepared in DI water under continuous stirring. The CNF concentration was selected based on previous optimization work in our laboratory, where 2.5% (wt/*v*) provided a suitable balance between structural reinforcement, rejection performance, and permeability [19]. MXene suspensions with different concentrations (0, 0.025, 0.05, and 0.1 wt/*v*%) were prepared in DI water under continuous stirring and sonication for 2 h to obtain homogeneous dispersions. A 2% (wt/*v*) polyethyleneimine (PEI) solution was also prepared by dissolving PEI in DI water and stirring for 15 min until a homogeneous mixture was obtained.

For the preparation of the membrane dope solution, 3 mL of the 3% κC solution was transferred into a container and maintained at 60 °C. Subsequently, 0.2 mL of the 2.5% CNF dispersion and 0.3 mL of the 2% PEI solution were added and mixed for 30 min to promote crosslinking and improve structural stability. Following this, 10 mL of the MXene suspension with the desired concentration was gradually introduced under continuous stirring and sonication to ensure uniform distribution.

A hydrophilic cellulose acetate (CA) filter paper with a pore size of 0.2 μm was used as the support layer. To enhance adhesion between the hydrogel layer and the support, 1 mL of 1% (wt/*v*) PEI solution was applied onto the CA surface and allowed to dry. PEI forms a cationic interlayer on the CA support layer via hydrogen bonding and electrostatic interaction with the polar groups on the CA filter. In turn, this will facilitate the interaction between the sulfate groups in κC and the amine groups in the PEI, hence improving interfacial adhesion and κC film anchoring [14]. The CA support was then placed at the bottom of a Sterlitech HP4750 dead-end filtration cell, and the prepared dope solution was cast under a hydraulic pressure of 5 bar for 2 h (Figure 1). The fabricated membrane was subsequently removed and dried at room temperature for 24 h to ensure structural stability. The compositions of the fabricated membranes are summarized in Table 3.

Table 3
Membrane type and dope compositions.

No.	Membrane	κC 3% wt/v (mL)	Mxene 10 mL (% wt/v)	PEI 2% wt/v (mL)	CNF 2.5% wt/v (mL)
1	κC	3	0	0.3	0.2
2	κC-MX.025	3	0.025	0.3	0.2
3	κC-MX.05	3	0.05	0.3	0.2
4	κC-MX.1	3	0.1	0.3	0.2

2.3. Filtration tests and PFAS sample preparation

The performance of the fabricated membranes was evaluated using pure water, model salt solutions, and PFAS-contaminated groundwater. Pure water flux experiments were conducted at ambient temperature using an HP4750 dead-end filtration unit (Sterlitech, USA) with a 300 mL feed chamber and an effective membrane area of 14.6 cm^2. Prior to data collection, membranes were compacted for 30 min to achieve steady-state conditions. The water flux (J) was calculated using Eq. (1), where V_p is the volume of permeate collected (L), A_m is the effective membrane area (m^2), and t is the filtration time (h):

$$J = \frac{V_p}{A_m * t} \quad (1)$$

Salt rejection experiments were performed using 1 g/L NaCl and $MgSO_4$ solutions prepared in deionized (DI) water. The rejection efficiency (R, %) was calculated using Eq. (2), where C_f and C_p represent the solute concentrations in the feed and permeate (mg/L), respectively:

$$R = \left(1 - \frac{C_p}{C_f}\right) * 100 \quad (2)$$

PFAS-contaminated groundwater collected from Williamtown (NSW, Australia) was used as the feed solution without further modification to represent realistic conditions. Filtration experiments were conducted at a constant pressure of 3 bar. All filtration experiments were performed in triplicate using independently prepared membrane samples. After selecting the optimised membrane, PFAS-contaminated groundwater filtration was conducted over three consecutive cycles, with each cycle tested in triplicate. Results are reported as mean ± standard deviation ($n = 3$). Heavy metal concentrations in feed and permeate samples were measured using inductively coupled plasma mass spectrometry (ICP-MS).

For PFAS analysis, feed and permeate samples were prepared following a dilution-based protocol adapted from ASTM D7979–17. Briefly, 2.5 mL of the supernatant was transferred into a 15 mL centrifuge tube, followed by the addition of 25 μL of isotopically labelled internal standard and 25 μL of surrogate standard (Wellington Laboratories). Then, 2.5 mL of methanol (MeOH) was introduced, and the mixture was vortexed for 2 min to ensure proper mixing. The sample was then filtered through a 0.22 μm regenerated cellulose (RC) filter, and 2.5 mL of the filtrate was transferred into a new 5 mL tube. Afterward, 5 μL of glacial acetic acid was added, followed by vortex mixing. Finally, 200 μL of the prepared sample was transferred into LC vials for PFAS concentration quantification by LC-MS/MS. TFA, 8:2 diPAP, PFBS, PFHxS, and PFOS were quantified separately using an Agilent 6546 A quadrupole time-of-flight mass spectrometer. For this analysis, water samples were diluted 1:1 (*v*/v) with methanol, followed by the addition of 20 μL of a 40 μg/L ^{13}C-labelled internal standard solution before

targeted analysis.

The antifouling performance of the membranes was evaluated using the same filtration setup. Initially, the pure water flux (J_{w0}) was measured, followed by filtration of PFAS-contaminated groundwater to obtain the permeate flux (J_f). The membranes were then rinsed with DI water, and the recovered water flux (J_{wr}) was measured. The reversible fouling (F_r), irreversible fouling (F_{ir}), total fouling (F_t), and flux recovery ratio (FRR) were calculated using Eqs. (3)–(6):

$$F_r\ (\%) = \left(\frac{J_{wr} - J_f}{J_{w0}}\right) \times 100 \quad (3)$$

$$F_{ir}\ (\%) = \left(\frac{J_{w0} - J_{wr}}{J_{w0}}\right) \times 100 \quad (4)$$

$$F_t\ (\%) = \left(1 - \frac{J_f}{J_{w0}}\right) \times 100 \quad (5)$$

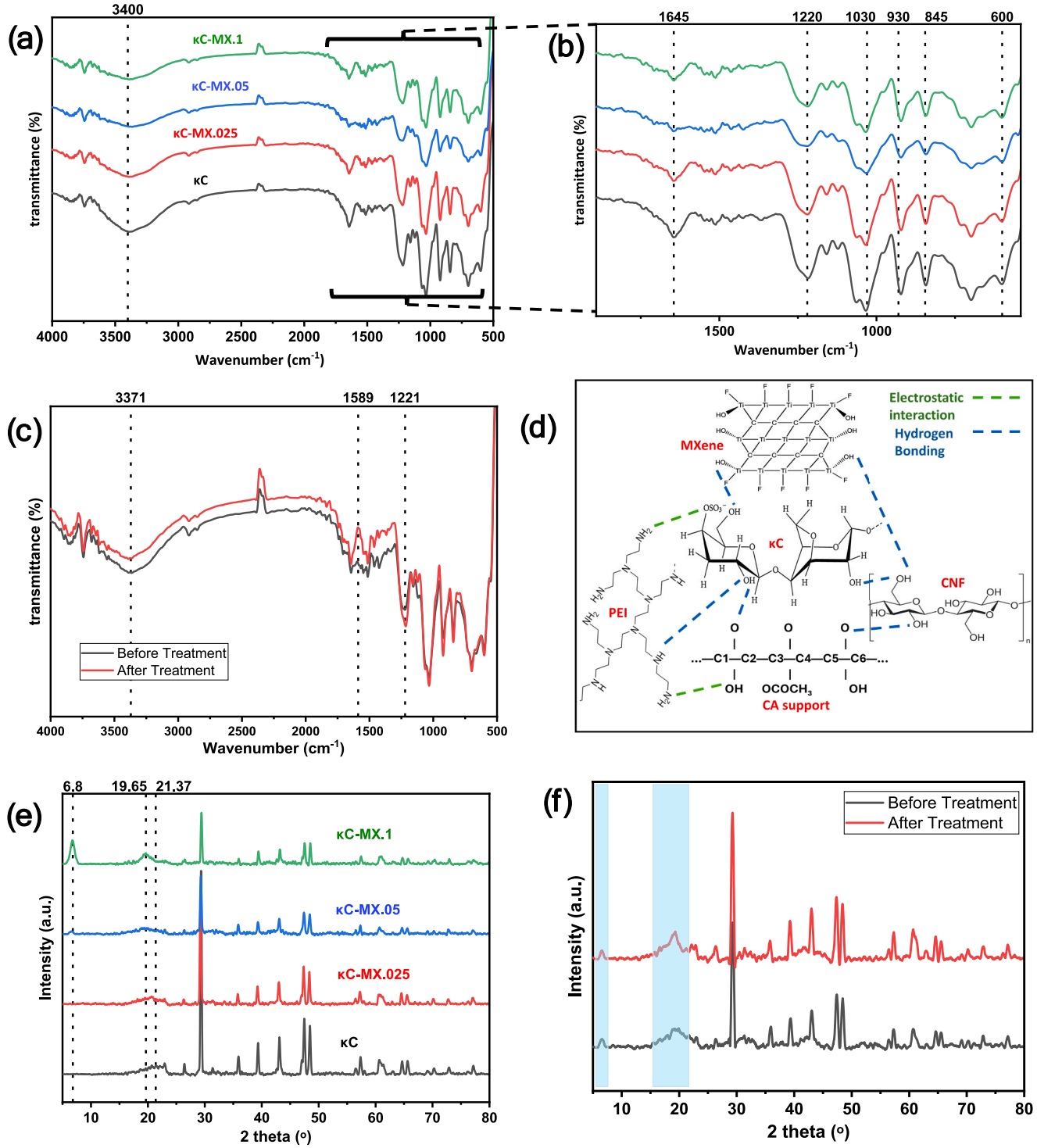


Fig. 2. (a) FTIR spectra of the neat κC-based membrane and MXene-incorporated membranes, (b) enlarged FTIR spectra in the 600–1700 cm^{-1} region, (c) FTIR spectra of κC-MX.05 before and after groundwater treatment, (d) schematic illustration of the proposed intermolecular interactions among the membrane components, (e) XRD patterns of κC and the MXene-containing membranes, and (f) XRD patterns of κC-MX.05 before and after groundwater treatment.

$$FRR\ (\%) = \left(\frac{J_{wr}}{J_{w0}}\right) \times 100 \quad (6)$$

2.4. Characterization methods

Fourier transform infrared spectroscopy (FTIR) examined the chemical structure of the prepared membranes using a Thermo Scientific Nicolet spectrometer coupled with an IR microscope (Thermo Fisher, Sydney, Australia) at an optical resolution of 0.9 cm^{-1}. Before testing, the samples were dried in an oven at 50 °C for 3 h. Spectra were collected over the wavenumber range of 4000–400 cm^{-1}, and the final spectrum for each sample was obtained by averaging three scans.

Surface and cross-sectional features of the membranes were observed using field-emission scanning electron microscopy (FESEM, Zeiss EVO LS15 SEM, Zeiss, Sydney, Australia). Prior to imaging, the membranes were dried and sputter-coated with a thin conductive layer to reduce surface charging. Elemental analysis was performed by energy-dispersive X-ray spectroscopy (EDX) using a Bruker SDD XFlash 5030 detector.

The crystalline characteristics of the membranes were studied by X-ray diffraction (XRD) using a Bruker D8 Discover diffractometer with Cu Kα radiation (λ = 1.5406 Å). Dried samples were scanned over a 2θ range of 5°–80°, and the interlayer spacing was determined using Bragg's law.

The hydrophilicity of the membrane surface was assessed by water contact angle measurements using the sessile drop method. The contact angle was measured at three different points on each sample, and the average value was reported. The surface charge of the membrane casting dispersions was evaluated by zeta potential analysis using a Nano-ZS Zetasizer (Malvern Analytical, UK) in deionized water at room temperature, and each result was reported as the average of six measurements.

Water absorption capacity was determined gravimetrically. Dry membrane samples were first weighed to obtain the initial mass, m_d, then immersed in distilled water for 24 h at room temperature. After removing excess water from the surface, the hydrated mass, m_w, was recorded. The water absorption percentage W_a was calculated as:

$$W_a(\%) = \frac{m_w - m_d}{m_d} \times 100 \quad (7)$$

The swelling behaviour was also evaluated by comparing the membrane thickness before and after immersion in water. The initial thickness L_i and the swollen thickness L_s were used to calculate the swelling index S_i according to:

$$S_i(\%) = \frac{L_s - L_i}{L_i} \times 100 \quad (8)$$

Membrane porosity was measured from the difference between the mass of the wet and dry samples. After soaking the membrane in deionized water, the saturated mass M_s was measured, followed by drying to a constant mass M_d. The porosity ε was determined by:

$$\varepsilon(\%) = \frac{M_s - M_d}{A \times \delta \times \rho_w} \times 100 \quad (9)$$

where A is the membrane area (cm^2), δ is the membrane thickness (cm), and ρ_w is the density of water, 1 g/cm^3.

The mean pore radius, r_m, was estimated from membrane porosity and pure water permeation data using the Guerout–Elford–Ferry relationship:

$$r_m = \sqrt{\frac{(2.9 - 1.75\varepsilon) \times 8\mu\delta Q}{\varepsilon A \Delta P}} \quad (10)$$

where μ is the viscosity of water (0.00089 Pa·s), Q is the volumetric flow rate of pure water (m^3/s), A is the effective membrane area, δ is the membrane thickness, ε is the membrane porosity, and ΔP is the applied transmembrane pressure.

The mechanical behaviour of the membranes was evaluated using a universal testing machine (LLOYD, AMETEK, UK) equipped with a 1 kN load cell. Rectangular membrane strips were fixed between the grips with a gauge length of 30 mm and tested at room temperature using a crosshead speed of 10 mm min^{-1}. Each sample was tested three times, and the tensile strength was obtained from the maximum load divided by the membrane cross-sectional area.

Thermogravimetric analysis (TGA) was performed using a NETZSCH STA 449 F5 Jupiter thermal analyzer. The membrane samples were heated from 30 to 800 °C at a heating rate of 10 °C/min under a nitrogen atmosphere. During the analysis, nitrogen was used as both the purge and protective gas, with flow rates of 50 and 20 mL/min, respectively. The mass loss of the samples was recorded as a function of temperature to evaluate their thermal stability and residual mass.

The concentrations of selected ions in the feed and permeate were measured by inductively coupled plasma mass spectrometry (ICP-MS, Agilent Technologies), while total organic carbon (TOC) was analyzed using a Shimadzu TOC analyzer.

PFAS analyses were performed with a Waters Xevo® TQ-XS quadrupole mass spectrometer in negative ion mode coupled with a Waters Acquity™ ultra-performance liquid chromatography (UPLC) I-class system (Waters Corporation, Sydney, Australia) fitted with the Waters PFAS analysis kit. The analytical column was a Waters ACQUITY UPLC I-class CSH Phenyl Hexyl (1.7 μm, 2.1 × 50 mm) maintained at 35 °C, with mobile phase A consisting of 95:5 deionized (DI) water: methanol +2 mM ammonium acetate and mobile phase B consisting of methanol +2 mM ammonium acetate. The isocratic program, calibration procedure, and quality control details are provided in the Supplementary Material. A subset of PFAS was quantified using an Agilent 6546 A quadrupole time-of-flight (qTOF) mass spectrometer, including compounds not measurable or affected by analytical limitations in the targeted LC–MS/MS method, as detailed in the Supplementary Material.

3. Results and discussions

3.1. Structural and morphological characteristics

3.1.1. FTIR and XRD

The FTIR spectra were used to assess the effect of MXene incorporation on the chemical structure of the κ-carrageenan membrane. The neat κC membrane showed the characteristic bands of κ-carrageenan, including a broad O—H stretching band around 3400 cm^{-1}, a sulfate ester band near 1220 cm^{-1}, a C–O/glycosidic vibration around 1030 cm^{-1}, and the characteristic peaks at approximately 930 and 845 cm^{-1}, which are assigned to 3,6-anhydrogalactose and D-galactose-4-sulfate, respectively [13,14].

After MXene incorporation, the characteristic κ-carrageenan bands remained visible, indicating that the main polymer structure was preserved. However, as shown in Fig. 2a and the enlarged view in Fig. 2b, noticeable changes in band intensity were detected at the main κC bands around 3400 cm^{-1} (O—H stretching), 1220 cm^{-1} (sulfate ester, S═O), 1030 cm^{-1} (C–O/glycosidic stretching), 930 cm^{-1} (3,6-anhydrogalactose), and 845 cm^{-1} (D-galactose-4-sulfate), indicating that MXene affected the local environment of the hydroxyl, sulfate, and glycosidic groups of κ-carrageenan. These changes suggest interactions between the –OH and $–SO_3^-$ groups of κC and the surface terminations of MXene, particularly –OH, —O, and —F. In particular, hydrogen bonding is likely to occur mainly between the hydroxyl groups of κC and the –OH/–O terminations of MXene, while the sulfate groups of κC may contribute through interfacial attraction with the functionalized MXene surface (Fig. 2d). Additional intensity changes were also observed around 600–700 cm^{-1}, corresponding to MXene-related low-wavenumber vibrations such as Ti–O/Ti–O–Ti-related modes, and near 1650 cm^{-1}, which is associated with bound water and hydroxyl-related interactions within the composite membrane [20,21].

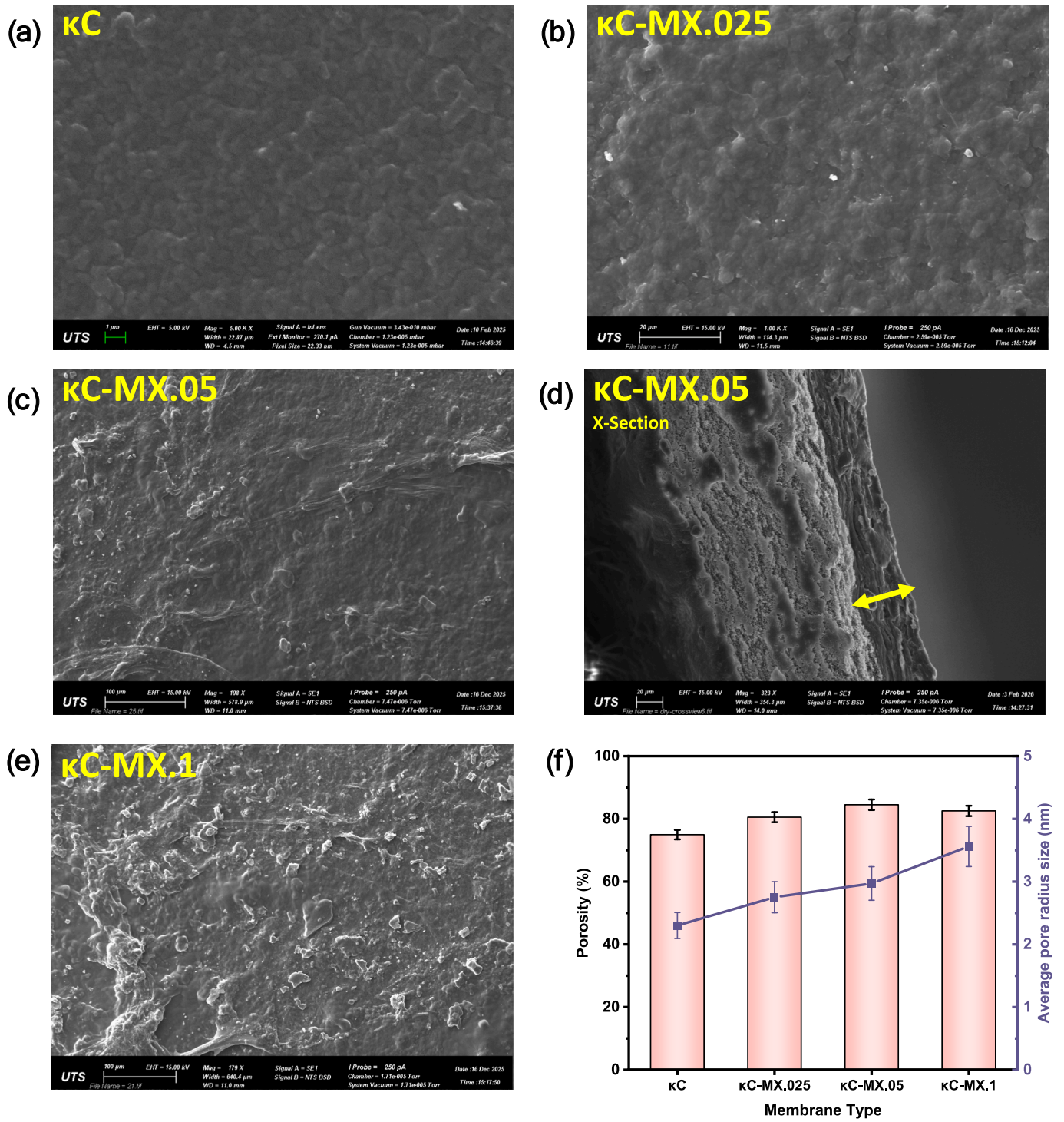


Fig. 3. Surface SEM micrographs of pristine κC and MXene-incorporated membranes: (a) κC, (b) κC-MX.025, (c) κC-MX.05(d) Cross-sectional SEM image of κC-MX.05, and (e) κC-MX.1. (f) Corresponding porosity and average pore radius values for the prepared membranes.

Among the prepared membranes, the sample containing 0.05 Mxene (κC-MX.05) showed the most pronounced spectral changes, indicating more effective interaction between MXene nanosheets and the κC matrix at this loading. This suggests that κC-MX.05 provided the most favorable MXene dispersion and interfacial contact within the polymer network, allowing stronger interaction between the functional groups of κC and the MXene surface terminations. At the higher loading of 0.1, the spectral effect became slightly less evident, which may be attributed to partial aggregation or restacking of MXene nanosheets, reducing the accessible surface area available for interaction with κC chains [22].

As shown in Fig. 2c, the FTIR spectra of the optimum membrane before and after groundwater treatment exhibited only minor changes in band intensity, with no meaningful shift in the main characteristic peaks. However, changes in band intensity were observed in several regions, particularly around 3371, 1589, 1221, and 932 cm^{-1}. The O—H band at 3371 cm^{-1} and the band at 1589 cm^{-1} became weaker after treatment, likely due to changes in hydrogen bonding and adsorption of groundwater constituents on the membrane surface. In contrast, the bands at 1221 and 932 cm^{-1}, assigned to sulfate ester groups and 3,6-anhydrogalactose units of κ-carrageenan, became more pronounced,

Table 4
EDX elemental content of the κC-MX.05 membrane before and after treatment.

Sample	Elemental content (wt%)					
	C	O	S	Na	Mg	Ca
κC-MX.05 before treatment	31.17	36.72	8.19	–	–	–
κC-MX.05 after treatment	27.91	45.48	9.62	0.52	0.03	1.35

indicating interfacial interactions with retained species. Overall, these changes suggest limited surface adsorption/deposition rather than severe membrane fouling.

As presented in Fig. 2e, the XRD patterns suggest some structural changes after MXene incorporation into the supported membrane system. The broad diffraction feature of the κC matrix slightly shifted to lower 2θ values, from 21.37° for neat κC to 20.62°, 19.8°, and 19.65° for the MXene-containing membranes, indicating a slight increase in average interchain spacing and altered chain packing within the membrane matrix [23]. In addition, a low-angle peak appeared at approximately 6.85°, corresponding to the characteristic (002) reflection of MXene and supporting its incorporation into the membrane [24]. Meanwhile, several reflections in the 35–50° region showed reduced intensity after MXene loading, suggesting minor changes in the ordering of the overall supported membrane system.

The XRD patterns before and after groundwater treatment, shown in Fig. 2f, were generally similar, with no new diffraction peaks and no major structural changes, indicating that the membrane remained largely stable during filtration. Only minor changes were observed in the existing peaks. In particular, the MXene-related low-angle peak shifted slightly from 6.59° to 6.55°, suggesting a small increase in d-spacing from approximately 1.34 to 1.35 nm based on Bragg's law. The broad diffraction feature of the κC-based membrane matrix also shifted from 19.9° to 19.32°, indicating a slight increase in average spacing and a minor change in chain packing. Overall, these subtle changes may be associated with water uptake or mild adsorption of groundwater constituents, but they do not indicate severe fouling or structural degradation of the membrane.

In addition, ICP-MS analysis showed that titanium (Ti), the principal metallic constituent of MXene, was below the analytical detection limit in both the groundwater feed and permeate samples. This indicates no detectable Ti in the analyzed permeate under the investigated filtration conditions, providing further supporting evidence of MXene retention during membrane operation.

3.1.2. SEM and EDX

The SEM images in Fig. 3 show morphological differences after MXene incorporation into the κC-based membrane. The neat κC membrane exhibited a relatively smooth and dense surface (See Fig. 3a). After MXene addition, the membrane surface became rougher and less uniform, indicating the incorporation of MXene into the active layer. At low loading (κC-MX.025), the surface remained fairly homogeneous, suggesting reasonable dispersion of MXene within the membrane matrix. At κC-MX.05, the surface became more textured, while at κC-MX.1,

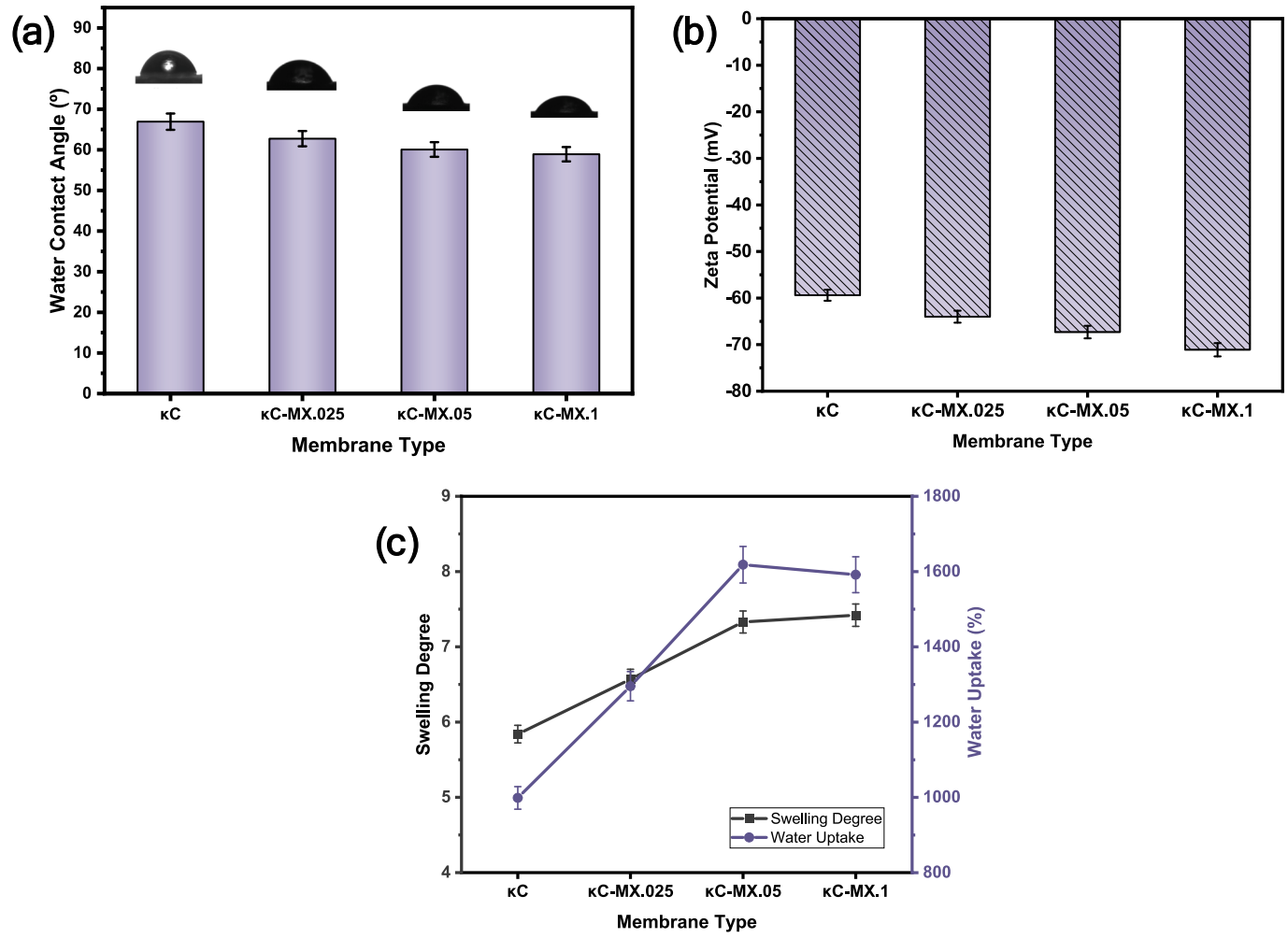


Fig. 4. (a) water contact angle, (b) zeta potential, and (c) Swelling degree and water uptake of the prepared membranes with 0.025, 0.05, and 0.1 (%wt/v) and without Mxene.

more irregular regions and clustered features were observed, indicating partial agglomeration or restacking at higher MXene loading. Such non-uniform regions may reduce membrane homogeneity and affect transport pathways [25].

The cross-sectional SEM image of κC-MX.05 revealed a distinct supported structure, consisting of a dense active layer formed on the porous CA support. The active layer appeared continuous and well adhered to the substrate, with no obvious delamination at the interface. The uppermost region of the CA support showed a gradual change in contrast, becoming more similar in shade to the overlying hydrogel layer, indicating partial interpenetration of the hydrogel phase into the top region of the support and suggesting intimate interfacial contact rather than a sharply delaminated boundary. The lamellar appearance of the selective layer was also consistent with the layered structure of MXene within the membrane [26]. The average thickness of the active layer, measured using ImageJ software, was approximately 34 μm. Overall, the SEM results confirm successful formation of the supported composite membrane and suggest that moderate MXene loading improved membrane structuring, while excessive loading led to partial agglomeration.

As shown in Table 4, EDX analysis after groundwater treatment revealed the presence of Na, Mg, and Ca on the membrane surface, indicating deposition of inorganic groundwater constituents during filtration. The sulfur and oxygen contents also increased after treatment, suggesting retention of sulfur-containing inorganic species on the membrane surface. Among the detected cations, Ca showed the highest accumulation, while Mg was present only in trace amounts. The increase in both S and Ca, and to a lesser extent Mg, may indicate sulfate-based inorganic fouling, possibly due to calcium sulfate or magnesium sulfate deposition. The higher Ca signal is also consistent with its relatively higher concentration in the groundwater. Overall, these results suggest mild inorganic fouling rather than severe membrane deterioration.

3.1.3. Pore size and porosity

The incorporation of MXene influenced both the porosity and average pore size of the membranes. The porosity increased from 74.96% for neat κC to 80.54% and 84.49% for κC-MX.025 and κC-MX.05, respectively, followed by a slight decrease to 82.54% for κC-MX.1. This trend suggests that MXene promoted the formation of a more open membrane structure at low to moderate loading, likely by disturbing polymer chain packing and increasing the free volume within the matrix. The hydrophilic surface terminations of MXene, such as –OH, —O, and —F, may also strengthen its interaction with the membrane components and contribute to a more homogeneous distribution of internal voids [27]. The slight decrease in porosity at the highest loading may be related to partial restacking or aggregation of MXene nanosheets, which could reduce the uniformity of pore formation [26].

The average pore size also increased slightly with MXene loading, from 2.30 nm for neat κC to 2.75 nm, 2.97 nm, and 3.56 nm for κC-MX.025, κC-MX.05, and κC-MX.1, respectively. The results suggest that MXene not only increased the overall void fraction at moderate loading but also slightly expanded the effective transport channels within the membrane. Such behaviour may be attributed to the two-dimensional structure of MXene nanosheets, which can act as spacers within the polymer network and reduce chain compaction. The simultaneous increase in porosity and pore size up to κC-MX.05 indicates the formation of a more open and accessible structure, while the continued increase in pore size at κC-MX.1, together with the slight drop in porosity, suggests that excessive MXene loading may have reduced structural uniformity. It should be noted that the reported average pore radii were estimated using the Guerout–Elford–Ferry relationship and should therefore be considered approximate values rather than direct measurements of the membrane pore structure.

3.2. Surface hydrophilicity and water interaction properties

3.2.1. Contact angle

The water contact angle of the membranes decreased gradually after MXene incorporation, indicating a moderate improvement in surface hydrophilicity. As shown in Fig. 4a, the neat κC membrane exhibited a contact angle of 66.93°, which decreased to 62.75°, 60.07°, and 58.92° for κC-MX.025, κC-MX.05, and κC-MX.1, respectively. This trend suggests that MXene contributed to a more wettable membrane surface. The decrease in contact angle is attributed to the hydrophilic nature of MXene, its -OH, —F, and -O-containing surface functionalities, enhanced surface area, improved pore structure and water channels, and its two-dimensional layered structure, which can improve surface interaction with water and modify membrane surface morphology. In addition, the good dispersion of MXene within the membrane matrix at low to moderate loading helped expose more hydrophilic sites on the surface.

3.2.2. Zeta potential

As shown in Fig. 4b, the neat κC membrane exhibited a zeta potential of −59.4 mV, which is attributed to the negatively charged sulfate groups of κ-carrageenan. After MXene incorporation, the zeta potential became progressively more negative, reaching −64.0 mV for κC-MX.025, −67.3 mV for κC-MX.05, and − 71.1 mV for κC-MX.1. This trend indicates that MXene increased the negative surface charge of the membranes. The increased negative charges are related to the negatively charged nature of titanium carbide MXene and its surface functionalities such as —O, —F, and –OH, which contributed additional negatively charged surface sites to the membrane. Although PEI was present in all

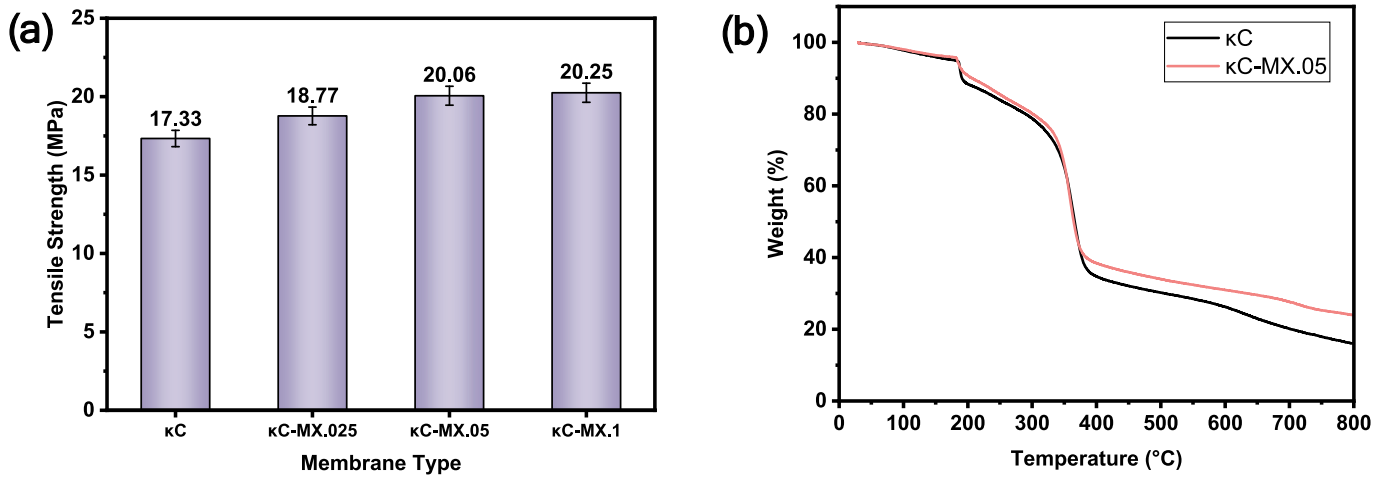


Fig. 5. (a) Tensile strength of the prepared membranes, and (b) TGA curves of neat κC and κC-MX.05 membranes.

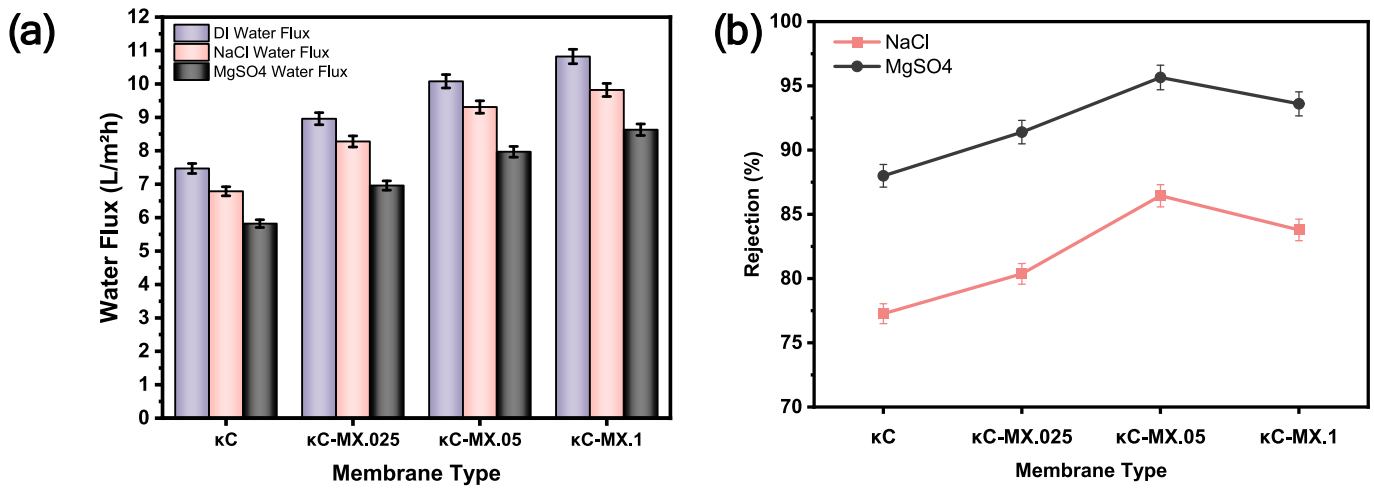


Fig. 6. (a) DI water, NaCl and MgSO4 water flux; (b) NaCl and MgSO4 (1 g/L) rejection. Filtration experiments were carried out at 3 bar and 25 °C.

membranes and could partially offset the negative charge through its amine groups, its amount was relatively low; therefore, the effect of MXene remained dominant, leading to a continuous shift toward more negative zeta potential with increasing loading. The strongly negative zeta potential of all membranes is also beneficial for improving electrostatic repulsion toward negatively charged species and reducing fouling by similarly charged contaminants [28].

3.2.3. Swelling degree and water uptake

The water uptake and swelling degree of the membranes increased after MXene incorporation, indicating improved hydrophilicity and enhanced interaction with water. As shown in Fig. 4c, the neat κC membrane exhibited a water uptake of 998.61% and a swelling degree of 5.84. After MXene addition, both values increased to 1295.39% and 6.57 for κC-MX.025, and further to 1618.19% and 7.33 for κC-MX.05, respectively. This behaviour suggests that MXene promoted water absorption and expansion of the membrane network, which may be attributed to its hydrophilic nature, oxygen-containing surface sites, and layered structure [27]. Hydrogen bonding between hydroxyl-containing groups in the membrane matrix and the hydrophilic surface functionalities of MXene likely contributed to the increased water uptake of the hydrogel. These features likely increased the affinity of the membrane toward water and disrupted dense chain packing, allowing easier penetration of water into the matrix. This behaviour may also be related to intermolecular interactions between MXene and the membrane components, particularly hydrogen bonding with hydroxyl-containing groups, which contributed to structural rearrangement and increased water accessibility within the matrix.

At the highest loading, κC-MX.1 showed a swelling degree of 7.42, while the water uptake decreased slightly to 1591.6%. This indicates that further MXene addition did not significantly improve the water-holding capacity of the membrane and may have reduced structural uniformity because of partial nanosheet aggregation or restacking [25].

3.3. Thermal and mechanical properties

The incorporation of MXene improved the tensile strength of the membranes. As shown in Fig. 5a, the neat κC-based membrane exhibited a tensile strength of 17.33 MPa, which is higher than the tensile strength previously obtained for a κC membrane without CNF in our earlier work (13.67 MPa) [14]. This improvement suggests that the incorporation of CNF contributed to strengthening the κC network, most likely through hydrogen bonding between the hydroxyl groups of CNF and κC, intermolecular entanglement and structural integrity while reducing pore collapse, as well as the reinforcing effect of the fibrous CNF structure within the polymer matrix. The tensile strength further increased to 18.77 MPa, 20.06 MPa, and 20.25 MPa for κC-MX.025, κC-MX.05, and κC-MX.1, respectively. This trend indicates that MXene provided additional mechanical reinforcement to the membrane. The improvement is related to the layered structure of MXene and its interfacial interactions with the membrane components, which can promote more effective stress transfer and improve structural cohesion [29]. These results are also consistent with the FTIR and XRD analyses, which suggested interactions between MXene and the membrane matrix as well as changes in chain packing after MXene incorporation.

Although the tensile strength continued to increase with MXene loading, the increment became smaller at higher loading, particularly between κC-MX.05 and κC-MX.1, suggesting that the reinforcement effect became less pronounced. Notably, the tensile test was conducted on the whole membrane, and hence the measured values include the combined effect of the active layer and the CA support.

The thermal behaviour of κC and κC-MX.05 membranes was evaluated by TGA, as shown in Fig. 5b. Both membranes exhibited a similar multi-stage weight-loss pattern, indicating that the incorporation of MXene did not substantially change the main thermal degradation pathway of the κC-based matrix. The first weight loss observed below approximately 150–180 °C can be attributed to the evaporation of physically adsorbed and bound water from the hydrophilic membrane structure. This behaviour is expected due to the presence of abundant hydroxyl and sulfate groups in κC, which can retain moisture within the polymer network. With increasing temperature, both membranes showed a major mass reduction in the intermediate temperature region, mainly associated with the decomposition of the κC polysaccharide backbone, including cleavage of glycosidic linkages and degradation of sulfate-containing groups. After the main degradation stage, the decomposition proceeded more slowly at higher temperatures [30].

Compared with the pristine κC membrane, κC-MX.05 retained a higher residual mass over the high-temperature region. At 800 °C, the residual mass of κC-MX.05 was approximately 24%, compared with about 16% for κC. This higher residue can be attributed to the inorganic nature of MXene and the possible interfacial interactions between MXene surface terminations, such as –OH, —O, and —F groups, and the hydroxyl and sulfate groups of κC through hydrogen bonding and electrostatic interactions. These interactions may restrict polymer chain mobility and promote the formation of more stable residual mass during thermal degradation. Therefore, MXene incorporation improved the high-temperature residual stability of the membrane, supporting the successful formation of a more thermally resistant κC-MX.05 composite structure.

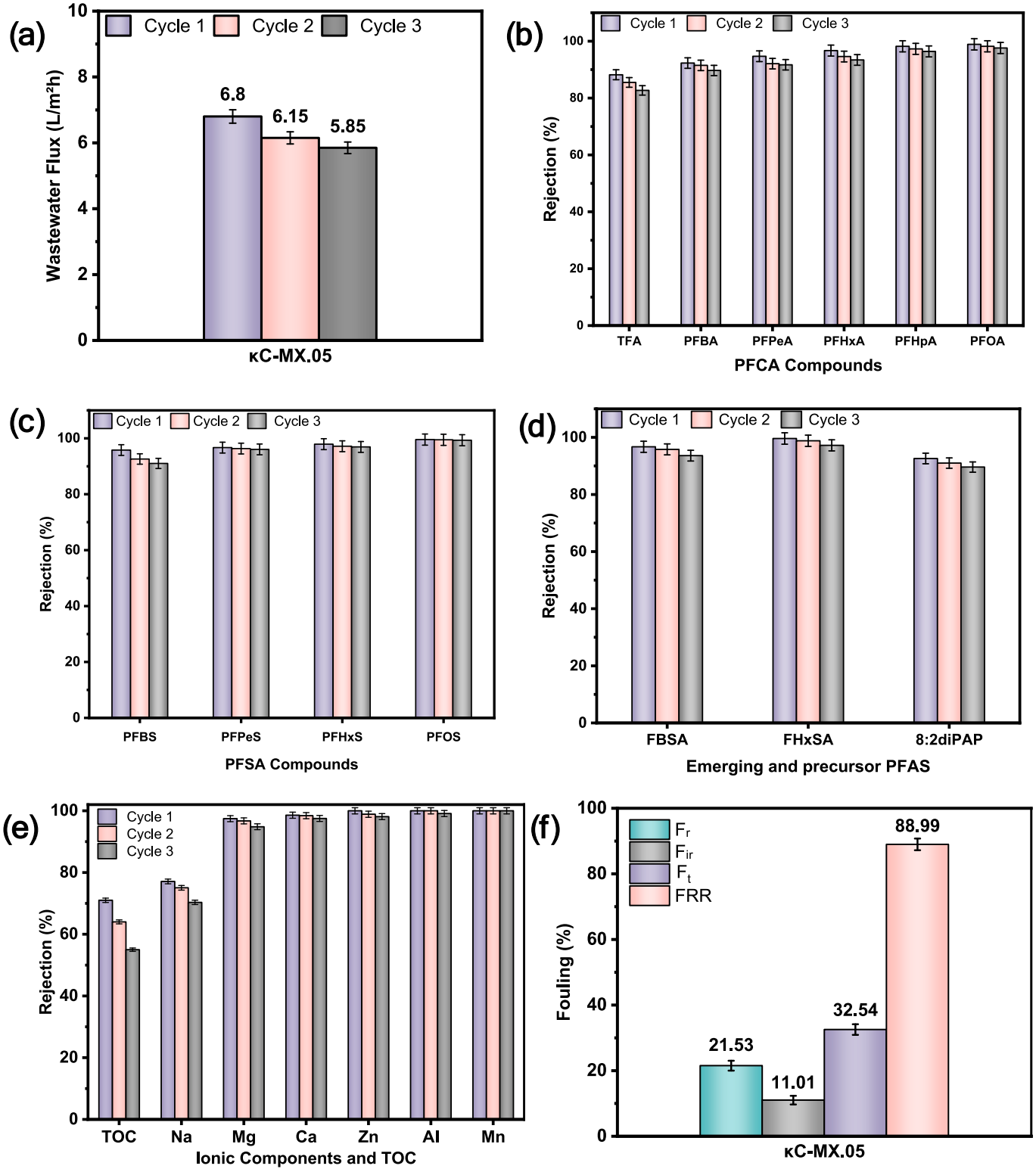


Fig. 7. Rejection performance of the κC-MX.05 membrane over three consecutive filtration cycles: (a) groundwater flux, (b) rejection of perfluoroalkyl carboxylic acids (PFCAs), (c) rejection of perfluoroalkyl sulfonic acids (PFSAs), (d) rejection of emerging and precursor PFAS, (e) rejection of ionic components and TOC, and (f) fouling measurements. Experiments were carried out at 3 bar and 25 °C.

3.4. Flux and ion separation performance as baseline evaluation

The pure water flux of the κC and κC-MX membranes was measured to evaluate the effect of MXene incorporation on baseline membrane transport performance. Before recording the flux values, the membranes were allowed to stabilize with DI water for 30 min. All experiments were conducted at 3 bar and 25 °C. As shown in Fig. 6a, the pure water flux increased from 7.47 ± 0.15 L/m^{2}h for neat κC to 8.96 ± 0.12, 10.08 ± 0.20, and 10.82 ± 0.14 L/m^{2}h for κC-MX.025, κC-MX.05, and κC-MX.1, respectively. This increase is consistent with the structural and

surface changes induced by MXene incorporation, including the decrease in water contact angle, the increase in water uptake and swelling degree (Fig. 4), the higher porosity, and the slight enlargement in average pore size (Fig. 3f). In addition, MXene is a two-dimensional hydrophilic material with tunable surface chemistry and interlayer structure, which can modify membrane transport pathways and water affinity [31]. The hydrogen-bonding interactions between κC/CNF hydroxyl groups and oxygen-containing surface sites on MXene likely reduced dense chain packing and generated a more accessible transport network. This interpretation agrees with the FTIR and XRD results, which indicated modification of the membrane network after MXene incorporation.

The flux measured using NaCl and $MgSO_4$ feed solutions followed the same overall trend but remained lower than the corresponding pure water flux. For NaCl, the flux increased from 6.79 ± 0.20 to 8.28 ± 0.15, 9.31 ± 0.12, and 9.82 ± 0.10 L/m^{2}h with increasing MXene loading, while for $MgSO_4$ it increased from 5.82 ± 0.14 to 6.96 ± 0.20, 7.97 ± 0.25, and 8.63 ± 0.16 L/m^{2}h. In all cases, the NaCl flux was higher than the $MgSO_4$ flux. This behaviour can be explained by the stronger transport resistance associated with $MgSO_4$. The hydrated radius of Na^+ is about 0.358 nm, whereas Mg^{2+} is larger at about 0.428 nm; similarly, Cl^- has a hydrated radius of about 0.332 nm, while SO_4^{2-} is larger at about 0.379 nm. The larger hydrated size and higher charge density of Mg^{2+} and SO_4^{2-} restrict water molecule transport through the membrane compared to Na^+ and Cl^- ions, which have a small hydration shell, leading to lower $MgSO_4$ flux. Besides, the greater viscosity of the $MgSO_4$ solution adversely impacts the water permeability. This trend can be explained by the combined influence of size exclusion and electrostatic interactions during ion transport through the membrane [32].

The rejection results shown in Fig. 6b further support this behaviour. For NaCl, the rejection increased from $77.27 \pm 1.50\%$ for neat κC to $80.37 \pm 1.00\%$ for κC-MX.025, reached a maximum of $86.45 \pm 1.25\%$ for κC-MX.05, and then decreased slightly to $83.79 \pm 1.15\%$ for κC-MX.1. A similar pattern was observed for $MgSO_4$, where the rejection increased from $88.00 \pm 1.00\%$ to $91.40 \pm 1.00\%$, then to $95.65 \pm 1.50\%$ for κC-MX.05, before declining to $93.60 \pm 1.00\%$ for κC-MX.1. The consistently higher rejection of $MgSO_4$ compared with NaCl is in agreement with the larger hydrated size and higher valence of Mg^{2+}/SO_4^{2-}, which are more strongly affected by steric hindrance and Donnan exclusion [33]. This interpretation is also supported by the zeta potential results, as the more negative membrane surface likely enhanced electrostatic exclusion of the more highly charged salt species and contributed to the higher $MgSO_4$ rejection up to κC-MX.05.

At κC-MX.1, the fluxes continued to increase, while NaCl and $MgSO_4$ rejection decreased slightly, indicating that further MXene addition favored permeability over selectivity. This trend is consistent with the slight decrease in porosity, the continued increase in pore size, and the more irregular surface morphology observed by SEM, suggesting that partial MXene restacking or less uniform distribution created transport pathways that enhanced water flow but slightly reduced ion rejection. The results show that increasing the MXene concentration from 0 to 0.05 (%wt/v) caused a proportional increase in the membrane average pore size, zeta potential, and membrane hydrophilicity. Consequently, the membrane water flux increased due to the higher surface hydrophilicity (lower contact angle) and expanded transport channels, while the rejection rate improved due to the enhanced negative surface charge that promoted the electrostatic repulsion of ions up to 0.05 (%wt/v) MXene loading. As MXene loading increased to 0.1 (%wt/v), water flux also increased as a result of greater membrane hydrophilicity and average pore radius, while membrane rejection declined due to enlarged pore radius. It is postulated that agglomeration of the MXene nanosheets occurred at higher MXene loading, resulting in a decline in membrane performance.

Overall, κC-MX.05 showed the best balance between permeability and separation. It delivered, at 3 bar, a pure water flux of 10.08 ± 0.20 L/m^{2}h, NaCl and $MgSO_4$ fluxes of 9.31 ± 0.12 and 7.97 ± 0.25 L/m^{2}h, respectively, together with the highest rejection values of $86.45 \pm 1.25\%$ for NaCl and $95.65 \pm 1.50\%$ for $MgSO_4$. Incorporating 0.05% (wt/v) of MXene into the developed membrane is justifiable, as this small amount led to significant improvements in both water flux (~ 37% increase) and rejection rate (8.69% to 11.89%) of the membrane.

3.5. Multi-contaminant wastewater treatment performance

3.5.1. PFAS removal

To further evaluate the practical performance of the optimal κC-MX.05 membrane, PFAS-contaminated groundwater was used as the feed solution. The main physicochemical characteristics of the groundwater are summarized in Table 1, while the concentrations of the detected PFAS are listed in Table 2. Filtration was conducted at 3 bar over three consecutive cycles. Due to the complex groundwater matrix, including dissolved salts and organic matter, the membrane exhibited a moderate initial flux of 6.80 ± 0.20 L/m^{2}h, which gradually decreased to 6.15 ± 0.14 and 5.85 ± 0.15 L/m^{2}h in the second and third cycles, respectively (Fig. 7a). This limited flux decline is consistent with mild surface-level fouling confirmed by EDX analysis, which showed Ca, Mg, and Na deposition alongside increased S and O signals attributable to the divalent cation-rich groundwater matrix, rather than structural degradation of the active layer as confirmed by FTIR and XRD.

The κC-MX.05 membrane demonstrated high rejection over three consecutive filtration cycles using PFAS-contaminated groundwater as the feed, encompassing ultra-short- to long-chain PFCAs, PFSAs, and precursor compounds at environmentally elevated concentrations ranging from approximately 1500 to 34,000 ng/L. PFAS transport was governed by electrostatic exclusion and Donnan effects, restricted diffusion through the hydrated active layer, and compound-specific interfacial interactions. This mechanistic framework is directly supported by the strongly negative zeta potential of −67.3 mV measured for κC-MX.05, substantially exceeding that of most commercial NF membranes (typically −20 to −40 mV), and reflecting the combined contribution of κC sulfate groups ($–OSO_3^-$) and MXene surface functionalities (—O, –OH) [34].

The feed pH of 5.8 governs the ionisation state of the target PFAS and is therefore central to the electrostatic exclusion mechanism. PFCAs and PFSAs have low pKa values and are expected to be predominantly deprotonated at pH 5.8, allowing electrostatic repulsion by the negatively charged membrane surface [35]. The precursor sulfonamides, by contrast, have considerably higher pKa values, typically in the range of 6 to 7, meaning that a measurable fraction of these compounds may remain in a neutral, non-ionised form. This reduces the contribution of electrostatic exclusion for this class relative to fully ionised PFCAs and PFSAs of comparable chain length.

As shown in Fig. 7b, within the PFCA group, rejection increased systematically with chain length, following the order TFA < PFBA < PFPeA < PFHxA < PFHpA < PFOA. TFA, despite its ultra-short chain and high aqueous mobility, was rejected at 88.2 ± 1.2, 85.5 ± 1.5, and $82.7 \pm 1.0\%$ across cycles 1–3. The negative membrane zeta potential suggests that electrostatic repulsion/Donnan exclusion contributed to its retention; however, due to the small size of TFA, restricted diffusion through the hydrated κC-MX hydrogel network and transport resistance within the dense active layer likely also played important roles. The slight decline over cycles indicates a modest reduction in retention, possibly due to changes in the hydrated network or partial occupation of interaction sites [9]. Short-chain PFCAs showed progressively stronger retention: PFBA decreased from 92.3 ± 1.1 to $89.7\% \pm 1.5$, PFPeA from 94.7 ± 1.6 to $91.7 \pm 1.2\%$, PFHxA from 96.7 ± 0.9 to $93.4 \pm 0.8\%$, and PFHpA from 98.2 ± 0.7 to $96.4 \pm 0.5\%$. The longer-chain PFCAs were strongly retained, with PFOA remaining between 98.9 ± 0.4 and $97.6 \pm 0.9\%$. For these longer-chain compounds, the higher rejection can be attributed to increased steric restriction within the hydrated

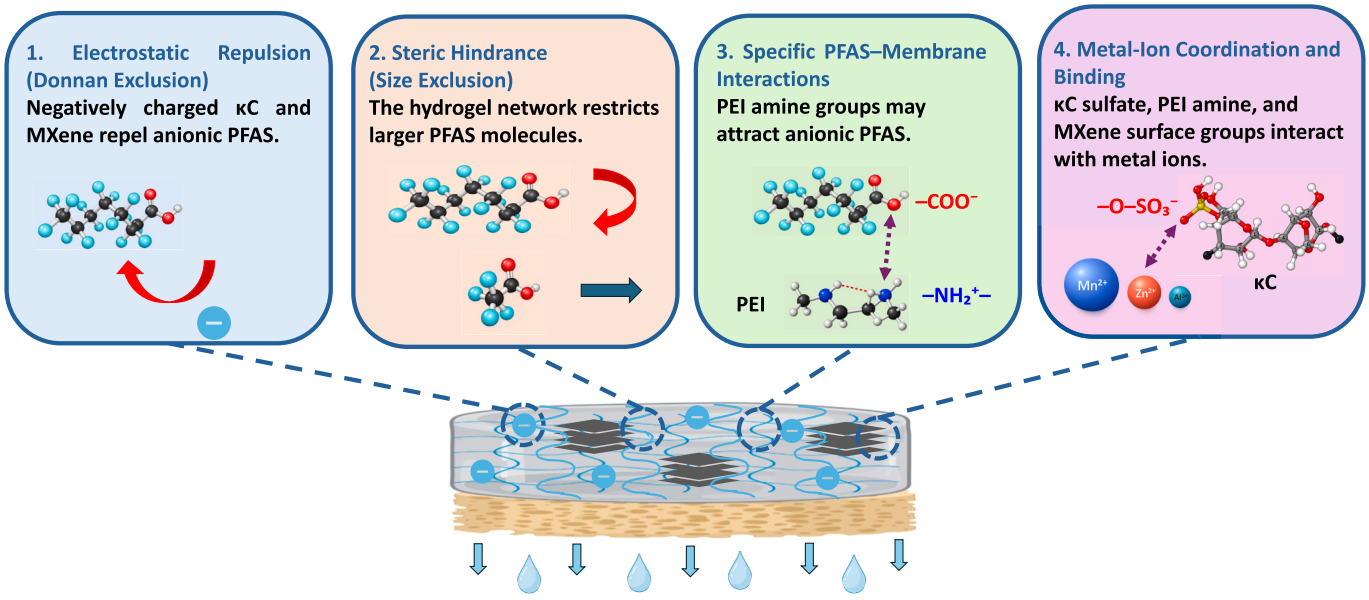


Fig. 8. A schematic illustration of the proposed separation mechanisms of the κC-MX.05 membrane for simultaneous PFAS and metal-ion removal. Electrostatic repulsion (Donnan exclusion) and steric hindrance are the main proposed PFAS rejection mechanisms, while specific PFAS–membrane interactions can provide additional contributions. Metal-ion removal also involves coordination and binding with membrane functional groups.

hydrogel membrane network and reduced aqueous-phase diffusivity with increasing PFAS chain length, acting alongside electrostatic exclusion [36,37].

As shown in Fig. 7c, the PFSA group showed uniformly stronger rejection than PFCAs of comparable chain length across all cycles. PFBS was rejected at 95.8 ± 1.2, 92.6 ± 0.9, and 91.0 ± 0.5%, and PFPeS at 96.7 ± 0.4, 96.3 ± 0.6, and 96.0 ± 0.7%, while PFHxS decreased from 97.9 ± 0.4 to 96.9 ± 0.5% and PFOS remained between 99.6 and 99.3 ± 0.2%. The superior PFSA performance is attributed to the strongly acidic sulfonate head group, which remains fully ionised at the feed pH of 5.8, resulting in strong electrostatic exclusion at the negatively charged membrane surface [38]. This head-group effect was most evident when comparing short-chain members of each class: despite similar molecular size, PFBS consistently outperformed PFBA across all cycles, reflecting the dominant role of charge rather than steric restriction at this size range.

As shown in Fig. 7d, precursor PFAS were also effectively rejected. FBSA decreased from 96.7 ± 0.7 to 93.6 ± 0.8% and FHxSA from 97.0 ± 0.2 to 94.3 ± 0.5%; the slightly higher retention of FHxSA is consistent with its longer fluorinated chain, larger molecular volume, and lower diffusivity, which increase steric restriction within the hydrated hydrogel network. The comparatively moderate rejection of the precursor sulfonamides relative to PFSAs of similar chain length also reflects their weaker ionisation at the feed pH. The polyfluoroalkyl phosphate diester 8:2 diPAP was rejected at 92.6 ± 1.0, 91.0 ± 0.8, and 89.6 ± 1.2%. Its retention is attributed to a combination of steric restriction and polar and hydrogen-bonding interactions between the phosphate diester functionality and membrane surface groups, including κC/CNF hydroxyl groups and MXene –O/–OH sites [39].

In a nutshell, the mechanisms of PFAS rejection are a combination of steric hindrance, electrostatic repulsion, and the influence of divalent ions in the feed solution. For the ultrashort-chain C2 TFA compound of small molecular size, membrane rejection is most likely due to Donnan repulsion between the negatively charged membrane surface and the carboxylate group, although this mechanism is compromised by the divalent ions in the solution that shield the negative charge of the membrane. Size exclusion, in contrast, plays an insignificant role in TFA rejection due to its small size. As for the short-chain C4 compounds, such as PFBA, PFBS, and FBSA, size exclusion becomes more effective alongside the electrostatic repulsion due to their larger molecular size, and hence, they demonstrated greater rejection than their counterpart ultrashort-chain C2 compounds. Notably, the C4 and C5 sulfonates (PFBS and PFPeS) exhibited greater rejection than their corresponding carboxylates (PFBA and PFPeA), which may be attributed to differences in head-group chemistry and their influence on electrostatic exclusion and steric interactions. Sulfoneamide compounds, e.g., FBSA, that exhibited outstanding rejection are probably due to hydrogen bonding with the PEI-crosslinked hydrogel matrix. PFAS compounds with a C5 to C7 carbon chain, e.g., PFPeA and PFHpA, exhibited a steady increase in rejection rate from 94.7% to 98.2% due to greater molecular length and volume of the fluorinated tail. As a result, steric hindrance by the membrane increased accordingly. For the long-chain PFAS compounds of the C8 carbon chain, like PFOA and PFOS, size exclusion is the dominant rejection mechanism due to their large molecular volume. In addition to steric hindrance, the hydrophobic nature of the C8 fluorinated tail drives these molecules out of the solution phase. Besides, the lower critical micelle concentration or tendency to form aggregates or complexes with divalent cations enhances their size and removal by the membrane. For polyfluoroalkyl phosphate esters, such as C8:2 diPAP, despite its large molecular weight, its rejection was lower than that of C8 perfluoroalkyl acid. Such behaviour is attributed to the flexible, bulky surfactant characteristics of the diPAP molecule.

The slight decline in rejection across the three cycles was linked to the composition of the groundwater matrix. The feed contained substantial divalent cation concentrations alongside high dissolved organic matter at a mildly acidic pH of 5.8. Divalent cations are known to compress the electrical double layer and partially screen membrane surface charge, reducing effective Donnan exclusion, particularly for small, charge-dependent PFAS [40]. Besides, the accumulation of organic matter on the membrane surface can shield the membrane's active sites. Together, these matrix effects provide a mechanistic basis for the inter-cycle rejection decline, which was most pronounced for the short-chain compounds whose rejection relies most heavily on electrostatic exclusion.

The main rejection mechanisms for Long-, short-, and ultrashort-chain PFAS compounds are attributed to specific interactions with the hydrated hydrogel, electrostatic repulsion (Donnan effect), and steric hindrance. The latter mechanism is less effective in the rejection and

removal of ultrashort-chain TFA because of their small size. MXene containing functional groups, such as hydroxyl, oxygen, and fluorine, boosts the negative charge and hence the electrostatic repulsion of PFAS compounds, while it enhances the antifouling properties of the membrane. The amine groups in PEI enhance the structural stability of the hydrogel backbone, control membrane swelling, and provide positive sites for the attraction of PFAS.

3.5.2. Ion rejection

Another set of experiments was performed at 3 bar over three consecutive filtration cycles to evaluate the rejection of TOC, major inorganic ions, and trace metal ions by the κC-MX.05 membrane, including Na^+, Mg^{2+}, Ca^{2+}, Zn^{2+}, Al^{3+}, and Mn^{2+} (Table 1). For the major inorganic ions, rejection followed the order Ca ≈ Mg > Na over all three cycles (Fig. 7e). In cycle 1, Na, Mg, and Ca rejections were 77.10 ± 1.20%, 97.45 ± 1.50%, and 98.57 ± 0.90%, respectively, and decreased gradually in the third filtration cycle to 70.32 ± 1.30%, 94.83 ± 1.60%, and 97.51 ± 1.00%. This trend is consistent with the lower valence, smaller hydrated size, and higher mobility of Na^+, which allow easier transport through the membrane, whereas Mg^{2+} and Ca^{2+} experience stronger electrostatic exclusion and greater transport resistance in the charged membrane environment [41]. The membrane contains κC sulfate groups, PEI amine groups, and MXene surface functionalities such as —O, –OH, and —F, all of which contribute to this selective ion transport [42].

For the trace metal ions, the membrane exhibited excellent removal performance over all three cycles. In cycle 1, Zn, Al, and Mn were almost completely rejected (≥99.99%). In cycle 2, Zn decreased slightly to 98.88 ± 0.40%, while Al and Mn remained at ≥99.99%. By cycle 3, rejection remained very high at 98.11 ± 0.5% for Zn, 99.11 ± 0.2% for Al, and ≥ 99.99% for Mn. These results indicate that the membrane maintained strong selectivity toward trace metal ions during repeated filtration, with only a very limited decline in performance. The high rejection of these ions was likely governed by the combined contribution of electrostatic exclusion and specific membrane–ion interactions. In particular, the sulfate groups of κC can participate in metal binding, for example:

$$Al^{3+} + 3\left(-OSO_3^-\right) \rightleftharpoons (-OSO_3)_3Al \quad (11)$$

In addition, MXene surface hydroxyl groups may provide further interaction sites, as illustrated by:

$$\equiv Ti - OH + Zn^{2+} \rightleftharpoons \equiv Ti - O - Zn^+ + H^+ \quad (12)$$

Together with coordination by PEI amine groups, these interactions likely contributed to the consistently high rejection of Zn, Al, and Mn throughout the three filtration cycles [14,42]. The proposed mechanisms contributing to the simultaneous removal of PFAS and metal ions are schematically illustrated in Fig. 8.

3.5.3. TOC reduction

As shown in Fig. 7e, the membrane exhibited moderate Total Organic Carbon (TOC) removal, with rejection decreasing from 71 ± 2% in the first cycle to 64 ± 2% in the second cycle and 55 ± 1% in the third cycle. Compared with the inorganic ions, the lower and less stable TOC rejection indicates that dissolved organic species were more difficult to retain consistently during repeated filtration. This gradual decline likely resulted from progressive accumulation of organic matter on the membrane surface and partial occupation of available interaction sites, which reduced the membrane's ability to remove dissolved organics over time. Nevertheless, the κC-MX.05 membrane maintained noticeable TOC removal over all three cycles.

3.6. Antifouling performance

Evaluating a membrane under idealised feed conditions reflects only part of the performance story. Real groundwater matrices introduce simultaneous fouling development from inorganic scaling, dissolved organic matter, and competing solutes that simple salt or dye solutions cannot replicate. The antifouling performance of κC-MX.05 was therefore assessed directly against PFAS-contaminated groundwater over three consecutive filtration cycles at a 50% recovery rate, with DI water rinsing between cycles at 3 bar and room temperature in dead-end filtration mode. While there is no standard for filtration cycles for long-term membrane performance, this method is consistent with previous studies [8,14]. The reason for this is also that the recovery rate, feed pretreatment, and membrane cleaning vary from study to study, making performance analysis unique for each study. Given the groundwater composition, fouling was expected to arise from two primary sources: inorganic scaling driven by the divalent cation-rich matrix and organic fouling from dissolved organic matter.

The membrane exhibited an initial DI water flux (J_{w0}) of 10.08 L/m^2h. During groundwater filtration, the groundwater flux (J_f) decreased from 6.80 ± 0.20 L/m^2h in the first cycle to 6.15 ± 0.14 and 5.85 ± 0.15 L/m^2h in the second and third cycles, respectively (Fig. 7a). After each cycle, DI water rinsing was performed to remove weakly adhered foulants, demonstrating the membrane's ability to recover performance.

Based on Eqs. (3) to (6), the FRR was 88.99%, indicating strong antifouling capability and effective cleaning by DI water alone. Fig. 7f presents F_t, F_r, and F_{ir} of the κC-MX.05 membrane. The F_t after three filtration cycles was 32.54%, with 21.53% attributed to F_r and 11.01% to F_{ir}. The relatively high F_r fraction indicates that a significant portion of foulants adhered loosely to the membrane surface and were successfully removed through DI water rinsing, while the low F_{ir} confirms the active layer was not permanently compromised during repeated filtration. This fouling profile is consistent with mainly reversible surface deposition, which is commonly observed in compact NF-type membranes and is generally more amenable to removal by simple rinsing than strongly irreversible fouling. The achieved FRR of 88.99% is also within the range reported for modified membranes treating complex water matrices [43,44].

Surface characterization confirmed the mild and non-destructive nature of the fouling. EDX revealed that Ca/Mg-SO4 deposition was consistent with inorganic scaling, while FTIR and XRD showed no new functional groups or crystalline phases, confirming that fouling was confined to surface-level deposition without chemical alteration or structural degradation of the active layer. The strong crosslinking of the hydrogel network via PEI and CNF, as well as the stable rejection performance and consistent FTIR/XRD spectra before and after wastewater filtration, indicate that the MXene was strongly anchored in the matrix with negligible leaching. Fig. 2c confirms no major shifts in the FTIR peaks before and after the filtration cycles. The FTIR results show minor intensity shifts in some regions, such as a tiny weakening of the O—H stretching band around 3371 cm^{-1} and the band at 1589 cm^{-1}, or minor changes around 1221 cm^{-1}, due to surface-level adsorption of groundwater constituents and hydrogen-bonding adjustments instead of structural degradation or damage.

The antifouling performance of κC-MX.05 is attributed to the synergistic contributions of its active layer components. The hydrophilic κC/CNF matrix, supported by CNF hydroxyl groups, forms a stable hydration layer acting as a physical and energetic barrier against foulant attachment. The strongly negative surface charge electrostatically repels anionic groundwater constituents, while MXene surface-terminated functional groups further enhance hydrophilicity and resistance to foulant deposition [45]. The combined result is a fouling profile dominated by reversible surface deposition, confirming the antifouling stability of κC-MX.05 for repeated groundwater treatment. Experiments also reveal that there was a decline in the water flux due to organic and inorganic fouling caused by the complex nature of the feed solution, while there was an insignificant decline in the rejection of metal ions and PFAS compounds as a result of membrane fouling. DI water cleaning

Table 5
Performance comparison of different membrane-based studies for PFAS removal.

Membrane /process	Pressure (bar)	Water flux (L/m^2h)	Feed type	Chain length	PFAS compound	Rejection (%)	Ref
NF270 / NF	Not reported	5	Ultra-filtered dam water	C4	PFBS	71	[38]
				C6	PFHxA	85	
				C6	PFHxS	78	
				C6 ether	GenX	94	
				C7	PFHpA	88	
				C8	PFOA	89	
				C8	PFOS	82	
				C9	PFNA	91	
				C10	PFDA	91	
TS80 / FO	4 + 25 (seawater osmotic pressure)	47.41	Groundwater	C1	TFMS	91.4	[8]
				C2	TFA	91	
				C3	PFPrA	92	
				C3	PFPrS	92.6	
				C6	PFHxA	96.9	
				C6	PFHxS	99.1	
				C7	PFHpA	98	
				C8	PFOA	99.3	
				C8	PFOS	~ 100 [a]	
				C9	PFNA	99.7	
				C10	PFDA	~100 [a]	
MOF-PDA-MXene-CA MMM / NF	3.5	6.2	Real hospital wastewater	C6	PFHxA	55	[46]
				C7	PFHpA	57	
				C8	PFOA	60	
AlFu MOF-PVA / MD	N.A.	~39	Landfill leachate	C4	PFBS	45	[47]
				C5	PFPeS	>99.4	
				C6	PFHxA	72.3	
				C6	PFHxS	91.3	
				C7	PFHpA	88.3	
				C7	PFHpS	>96.8	
				C8	PFOA	93.5	
				C8	PFOS	90.0	
NF270 / NF	9.7	Not reported	Spiked artificial groundwater	C4	PFBA	>94	[51]
				C4	PFBS	>99	
				C5	PFPeA	>97	
				C6	PFHxA	>95	
				C6	PFHxS	>99	
				C8	PFOA	>97	
				C8	PFOS	>99	
				C9	PFNA	>98	
				C10	PFDA	>97	
CS/GA hydrogel-assisted PA / NF	4	16.1/bar	PFAS-spiked tap water	C4	PFBA	~83	[48]
				C4	PFBS	~89	
				C6	PFHxS	~98	
				C8	PFOS	~98	
				C9	PFNA	~97	
				C10	PFDA	~98	
ZIF-L/PEI TFN / NF	3	47.56/bar	PFAS-spiked DI water	C4	PFBA	35.47	[49]
				C4	PFBS	47.92	
				C6	PFHxA	81.52	
				C6	PFHxS	87.85	
				C8	PFOA	95.85	
				C8	PFOS	98.47	
				C9	PFNA	~100 [a]	
NF90 /NF	8	120.4	Synthetic groundwater	C4	PFBA	~97.2	[52]
				C4	PFBS	~98	
				C6	PFHxS	~98.1	
				C8	PFOA	~97.8	
				C8	PFOS	~89.9	
MXene–polyamide thin-film nanocomposite (*MXene-TFN*) / NF	4.5	29.26 (pure water flux)	PFOS-spiked DI water	C8	PFOS	97.6	[45]
β-Cyclodextrin modified graphene oxide (GO-βCD) / NF	2	25/bar	PFAS-spiked DI water	C4	PFBA	89	[50]
				C5	PFPeA	93	
				C6	PFHxA	95	
				C8	PFOA	99	

(*continued on next page*)

Table 5 (*continued*)

Membrane /process	Pressure (bar)	Water flux (L/m^2h)	Feed type	Chain length	PFAS compound	Rejection (%)	Ref
Ag-MOF/PA (DS-MOF) / NF	6	16.1 (L/m^2h/ bar)	PFOA-spiked DI water	C8	PFOA	93.4	[53]
PES-MOF 303-TFC / NF	5	11.68 (L/m^2h/ bar)	Simulated groundwater	C8	PFOA	91.77	[54]
				C8	PFOS	93.4	
κC-MX.05 / NF	3	6.8	Real groundwater	C2	TFA	88.2	This work
				C4	PFBA	92.3	
				C4	PFBS	95.8	
				C4	FBSA	96.7	
				C5	PFPeA	94.7	
				C5	PFPeS	96.7	
				C6	PFHxA	96.7	
				C6	PFHxS	97.9	
				C6	FHxSA	97.0	
				C7	PFHpA	98.2	
				C8	PFOA	98.9	
				C8	PFOS	≥99.6	
				C8:2	8:2 diPAP	92.6	

[a] ~100% indicates concentrations below analytical limits, not complete absence.
Note: PFAS compounds not reported for the present membrane were below detection or quantification limits in the tested groundwater.

is probably insufficient, particularly with wastewater feed solution, and more advanced pretreatment is recommended to reduce membrane fouling.

3.7. Performance comparison

The performance of the κC-MX.05 membrane was compared with laboratory-prepared and commercial membranes (Table 5). A key distinction of this study is the superior treatment of real PFAS-contaminated groundwater from the Williamtown RAAF site, unlike many benchmark membranes tested on PFAS spiked in DI water, reflecting its performance in a complex environment. This groundwater represents a chemically complex and environmentally relevant matrix containing multiple PFAS, metal ions, organic matter, and co-contaminants that can influence membrane separation through charge screening, competitive transport, adsorption-site occupation, fouling, and concentration polarization. Under these challenging conditions, κC-MX.05 demonstrated competitive rejection across a broad range of PFAS compounds, encompassing ultra-short-, short-, and long-chain compounds spanning from C2 to C8. The membrane demonstrated excellent rejection of heavy metals and a broad spectrum of PFAS compounds, ranging from ultrashort- to long-chain derivatives. The lower water flux of the κC-MX.05 is attributed to its tight selective structure, which is essential for efficient blockage of small and highly mobile ultrashort-chain PFAS that breach looser NF membranes. Compared to previous investigations using laboratory membranes [45–50], this study demonstrated a competitive rejection of various PFAS compounds, utilizing real contaminated groundwater. Besides, the membrane uses biodegradable materials, offering a sustainable alternative to petroleum-based polymer membranes.

Among commercial NF membranes, NF270 showed notably lower rejection for short-chain compounds, with PFBS at 71% and PFHxS at 78% in ultra-filtered dam water. In contrast, κC-MX.05 achieved 95.8 ± 1.2% for PFBS and 97.9 ± 0.4% for PFHxS, alongside 92.3 ± 1.1%, 94.7 ± 1.6%, and 96.7 ± 0.9% for PFBA, PFPeA, and PFHxA, respectively, in real groundwater of a significantly more challenging matrix. This superior short-chain performance reflects the strongly negative surface charge of κC-MX.05 (−67.3 mV), driving Donnan exclusion for small anionic PFAS that cannot be retained by size exclusion alone.

The 88.2 ± 1.2% rejection of TFA is particularly noteworthy given its ultra-short chain, high aqueous mobility, and negligible hydrophobic affinity. Only the TS80 forward osmosis membrane reports TFA rejection in the table at 91%, achieved through osmotic rather than hydraulic pressure. The comparable TFA rejection by κC-MX.05 at only 3 bar confirms that charge-based exclusion and restricted transport within the hydrogel matrix governed the removal of this compound.

Compared with recently developed nanocomposite membranes, κC-MX.05 outperformed the ZIF-L/PEI TFN membrane, which achieved only 35.47% for PFBA and 47.92% for PFBS in spiked DI water, and the MOF-PDA-MXene cellulose acetate membrane, which achieved only 55 to 60% for PFHxA to PFOA in real hospital wastewater. Although high-pressure commercial membranes such as NF90 achieved high rejection at 8 bar, κC-MX.05 achieved broad PFAS rejection at only 3 bar in real contaminated groundwater. Notably, κC-MX.05 is the only membrane in Table 5 fabricated primarily from naturally derived biopolymer components, including κ-carrageenan and cellulose nanofibers. This distinguishes it from commercial polyamide and fully synthetic polymer-based membranes and, together with its low-pressure operation, positions it as a promising biopolymer-based alternative for PFAS-impacted groundwater treatment.

Unlike commercial membranes that require high operating pressures or are tested only on synthetic wastewater, the proposed hydrogel membrane provides simultaneous, high-efficiency rejection of a broad range of carbon-chain PFAS compounds and heavy metals from contaminated groundwater at a low operating pressure of 3 bar. Furthermore, the developed membrane uses natural biopolymers (k-C and CNF) as an alternative sustainable and eco-friendly option that aligns with global environmental goals.

4. Conclusion

In this study, a κ-carrageenan (κC)-based composite hydrogel membrane incorporating cellulose nanofibers (CNF), polyethyleneimine (PEI), and MXene nanosheets was developed and evaluated for the treatment of PFAS-contaminated groundwater. The effect of MXene loading (0, 0.025, 0.05, and 0.1 wt%) on membrane structure, physicochemical properties, and separation performance was systematically investigated, with κC-MX.05 identified as the optimum formulation, providing the best balance between water permeability and selectivity among the tested loadings while maintaining a well-structured active layer with enhanced hydrophilicity, surface charge, mechanical and thermal strength.

The optimum κC-MX.05 membrane achieved a pure water flux of 10.08 L/m^2h, NaCl rejection of 86.45%, and $MgSO_4$ rejection of 95.65%. The higher rejection of divalent $MgSO_4$ relative to NaCl reflected the

dominance of electrostatic exclusion driven by the strongly negative surface charge (−67.3 mV). When evaluated against PFAS-contaminated groundwater, the membrane demonstrated high rejection across a broad and structurally diverse PFAS panel, encompassing ultra-short- to long-chain PFCAs, PFSAs, and precursor compounds at environmentally elevated concentrations. Importantly, this evaluation was conducted using real AFFF-impacted groundwater from the Williamtown RAAF site, representing an environmentally realistic and chemically complex matrix containing multiple PFAS, inorganic ions, divalent cations, organic matter, and co-contaminants. Rejection followed the order TFA < PFBA < PFPeA < PFHxA < PFHpA < PFOA for PFCAs, with PFSAs consistently outperforming PFCAs of equivalent chain length due to stronger electrostatic exclusion of the sulfonate head group. PFHxS rejection remained above 96.9%, while PFOS rejection remained above 99.3% across all three cycles. The rejection mechanism was governed by electrostatic exclusion as the dominant driver for short-chain PFAS, while the higher retention of longer-chain compounds was attributed to combined electrostatic exclusion, steric restriction, and reduced aqueous-phase diffusivity within the hydrated hydrogel network. Simultaneous removal of groundwater co-constituents was also achieved, with Zn, Al, and Mn rejected at 98–≈100% and Ca and Mg showing higher rejection than Na across all cycles. The membrane also demonstrated promising antifouling stability over three consecutive filtration cycles, achieving an FRR of 88.99% with DI water rinsing alone, confirming that the active layer was not permanently compromised under repeated groundwater filtration.

Overall, κC-MX.05 demonstrated promising performance as a low-pressure, sustainable alternative for PFAS-contaminated groundwater treatment, combining broad-spectrum PFAS rejection, simultaneous co-contaminant removal, and antifouling stability. Future work should focus on scaling the membrane fabrication process, the biodegradation behaviour of the membrane after use and the potential of alternative green crosslinkers to replace PEI, which also warrants further investigation. Additionally, nanoscale water transport and PFAS-membrane interactions could be explored through molecular dynamics simulations or related atomistic modelling to provide deeper mechanistic insight into the selective rejection behaviour observed in this study.

Declaration of competing interest

The authors declare that they have no known competing financial interests or personal relationships that could have appeared to influence the work reported in this paper.

Acknowledgement

This research is made possible by a food security research award (MME04-0607-230061) from the Qatar National Research Fund (QNRF) in partnership with the Ministry of Municipality.

Appendix A. Supplementary data

Supplementary data to this article can be found online at https://doi.org/10.1016/j.seppur.2026.140937.

Data availability

Data will be made available on request.

References

[1] M. Greger, T. Landberg, Removal of PFAS from water by aquatic plants, J. Environ. Manag. 351 (2024) 119895.
[2] M. Currell, N. Northby, P. Netherway, Examining changes in groundwater PFAS contamination from legacy landfills over a three-year period at Australia's largest urban renewal site, Chemosphere 352 (2024) 141345.
[3] F. Dixit, et al., PFAS removal by ion exchange resins: a review, Chemosphere 272 (2021) 129777.
[4] S. Das, A. Ronen, A review on removal and destruction of per- and polyfluoroalkyl substances (PFAS) by novel membranes, Membranes 12 (7) (2022).
[5] G.S. Casella, et al., Recent developments in membrane treatment technologies for PFAS removal from surface and groundwater, J. Environ. Chem. Eng. 14 (1) (2026).
[6] C.J. Liu, T.J. Strathmann, C. Bellona, Rejection of per- and polyfluoroalkyl substances (PFASs) in aqueous film-forming foam by high-pressure membranes, Water Res. 188 (2021) 116546.
[7] F.A. Zeidabadi, E.B. Esfahani, M. Mohseni, Effects of water matrix on per- and polyfluoroalkyl substances (PFAS) treatment: physical-separation and degradation processes – a review, J. Hazardous Mater. Adv. 10 (2023).
[8] Y. Aedan, et al., PFAS-contaminated groundwater treatment by forward osmosis using pressure-stimuli-responsive nanofiltration membrane: effects of chain length and operating conditions, Desalination 617 (2026).
[9] Y. Zhi, et al., Enhancing rejection of short-chain per- and polyfluoroalkyl substances by tailoring the surface charge of nanofiltration membranes, Water Res. 272 (2025) 122931.
[10] A. Safulko, et al., Rejection of perfluoroalkyl acids by nanofiltration and reverse osmosis in a high-recovery closed-circuit membrane filtration system, Sep. Purif. Technol. 326 (2023).
[11] J. Ma, et al., MXene (Ti3T2CX)-reinforced thin-film polyamide nanofiltration membrane for short-chain perfluorinated compounds removal, Process. Saf. Environ. Prot. 168 (2022) 275–284.
[12] E. Karbassiyazdi, et al., Gravity-driven composite cellulose acetate/activated carbon aluminium-based hydrogel membrane for landfill wastewater treatment, Chem. Eng. Res. Des. 200 (2023) 682–692.
[13] R. Kardani, et al., Eco-friendly kappa-carrageenan-nano zerovalent iron hydrogel water and wastewater purification, J. Hazard. Mater. 492 (2025) 138123.
[14] R. Kardani, et al., Nanocomposite kappa-carrageenan-GO/PEI membrane for wastewater valorization and metals recovery, Chem. Eng. J. 523 (2025).
[15] S. Mohammed, J. Aburabie, R. Hashaikeh, A review on the potential of cellulose nanomaterials for the development of thin film composite polyamide membranes for water treatment, Chemosphere 363 (2024) 142927.
[16] N. Albayati, et al., A comprehensive review on the use of Ti3C2Tx MXene in membrane-based water treatment, Sep. Purif. Technol. 345 (2024).
[17] I. Ihsanullah, M. Bilal, Potential of MXene-based membranes in water treatment and desalination: a critical review, Chemosphere 303 (Pt 3) (2022) 135234.
[18] Defence, A.G.D.o, *RAAF Base Williamtown PFAS Community Update: October* 2022*: PFAS Remediation and Management Update*. 2022, Department of Defence, Australian Government: Australia. p. 4, 2022.
[19] L. Alsaka, et al., Fabrication of kappa carrageenan-cellulose nanofiber/graphene oxide composite membrane for water purification, J. Environ. Chem. Eng. 13 (6) (2025).
[20] S. Tu, et al., Large dielectric constant enhancement in MXene percolative polymer composites, ACS Nano 12 (4) (2018) 3369–3377.
[21] M. Jakubczak, et al., The role of $Ti_3C_2T_x$ MXene in hydrogel engineering for structural organization and ROS scavenging in bacterial models, New J. Chem. 49 (35) (2025) 15129–15144.
[22] J. FitzPatrick, Y. Gogotsi, MXene polymer composites: a review, MRS Bull. 50 (11) (2025) 1351–1363.
[23] Akira Shimazu, T.M., Kenichi Ikeda, Interpretation of d-spacing determined by wide angle X-ray scattering in 6FDA-based polyimide by molecular modeling, J. Membr. Sci. 166 (2000) 113–118.
[24] M. Yadav, M. Kumar, A. Sharma, Review of $Ti_3C_2T_x$ MXene nanosheets and their applications, ACS Appl. Nano Mater. 7 (9) (2024) 9847–9867.
[25] M. Carey, M.W. Barsoum, MXene polymer nanocomposites: a review, Mater. Today Adv. 9 (2021).
[26] K. Gong, et al., MXene as emerging nanofillers for high-performance polymer composites: a review, Compos. Part B 217 (2021).
[27] M.S. Ali, et al., Recent progress on MXene-polymer nanocomposites and their applications, Sustain. Mater. Technol. 45 (2025).
[28] Y. Sun, et al., MXene-based membranes in water treatment: current status and future prospects, Sep. Purif. Technol. 331 (2024).
[29] M. Liu, et al., Deformation of and interfacial stress transfer in Ti(3)C(2) MXene-polymer composites, ACS Appl. Mater. Interfaces 14 (8) (2022) 10681–10690.
[30] Y. Zhou, et al., Preparation and characterization of kappa-carrageenan modified with maleic anhydride and its application in films, Mar. Drugs 19 (9) (2021).
[31] O. Kwon, et al., A comprehensive review of MXene-based water-treatment membranes and technologies: recent progress and perspectives, Desalination 522 (2022).
[32] N.S. Suhalim, et al., Rejection mechanism of ionic solute removal by nanofiltration membranes: an overview, Nanomaterials 12 (3) (2022).
[33] K. Takeuchi, et al., Salt rejection behavior of carbon nanotube-polyamide nanocomposite reverse osmosis membranes in several salt solutions, Desalination 443 (2018) 165–171.
[34] H.-y. Guo, et al., Ion adsorption on nanofiltration membrane surface and its effect on rejection of charged solutes: a zeta potential approach, Sep. Purif. Technol. 326 (2023).
[35] F. Dixit, et al., Evaporative losses of perfluoroalkyl Sulfonamides during PFAS analysis, ACS Omega 11 (9) (2026) 14638–14643.
[36] Leniz-Pizarro, F., et al., Dual-functional nanofiltration and adsorptive membranes for PFAS and organics separation from water. ACS ES&T Water, 2022. 2(5): p. 863–872.

[37] J.R. Gauthier, S.A. Mabury, Experimentally determined aqueous diffusion coefficients of PFAS using 19F NMR diffusion-ordered spectroscopy, ACS ES&T Water 4 (10) (2024) 4615–4624.
[38] T. Fujioka, et al., Effects of functional groups of polyfluoroalkyl substances on their removal by nanofiltration, Water Res. X 24 (2024) 100233.
[39] C. Liu, et al., Removal of per- and polyfluoroalkyl substances by nanofiltration: effect of molecular structure and coexisting natural organic matter, J. Hazard. Mater. 454 (2023) 131438.
[40] C. Zhao, et al., Efficient removal of perfluorooctane sulphonate by nanofiltration: insights into the effect and mechanism of coexisting inorganic ions and humic acid, J. Membr. Sci. 610 (2020).
[41] B. Tansel, et al., Significance of hydrated radius and hydration shells on ionic permeability during nanofiltration in dead end and cross flow modes, Sep. Purif. Technol. 51 (1) (2006) 40–47.
[42] K. Kalaiselvi, et al., Adsorption of Pb2+ ions from aqueous solution onto porous kappa-carrageenan/cellulose hydrogels: isotherm and kinetics study, Sustainability 15 (12) (2023).
[43] A.S. Maraddi, et al., CoFe₂O₄ modified bentonite-based mixed matrix loose nanofiltration membranes for effective wastewater treatment, Chemosphere 350 (2024) 141051.
[44] N.N.R. Ahmad, et al., An overview of the modification strategies in developing antifouling nanofiltration membranes, Membranes (Basel) 12 (12) (2022).
[45] T. Le, et al., Functionalized-MXene thin-film nanocomposite hollow Fiber membranes for enhanced PFAS removal from water, ACS Appl. Mater. Interfaces 14 (22) (2022) 25397–25408.
[46] S.A. Minhas, et al., MOF/polydopamine-modified MXene based mixed matrix membrane for per- and polyfluoroalkyl substances removal from real wastewater, Sep. Purif. Technol. 370 (2025).
[47] J. Zhang, et al., Study of MOF incorporated dual layer membrane with enhanced removal of ammonia and per−/poly-fluoroalkyl substances (PFAS) in landfill leachate treatment, Sci. Total Environ. 806 (Pt 4) (2022) 151207.
[48] X. Wang, et al., Enhancement separation selectivity of mineral ions and perfluorinated and polyfluoroalkyl substances by nanofiltration membrane through hydrogel-assisted interfacial polymerization, Water Res. 280 (2025) 123498.
[49] Y. Bi, et al., A novel ZIF-L/PEI thin film nanocomposite membrane for removing perfluoroalkyl substances (PFASs) from water: enhanced retention and high flux, Sci. Total Environ. 925 (2024) 171727.
[50] E. Mahofa, et al., Manipulating intrapore energy barriers in graphene oxide nanochannels for targeted removal of short-chain PFAS, ACS Nano 19 (15) (2025) 14742–14755.
[51] T.D. Appleman, et al., Nanofiltration and granular activated carbon treatment of perfluoroalkyl acids, J. Hazard. Mater. 260 (2013) 740–746.
[52] J. Cao, et al., PFAS removal from reverse osmosis and nanofiltration brine by granular activated carbon: thermodynamic insights into salinity effects, Water Res. 282 (2025) 123758.
[53] M. Pilevar, et al., Customizing surface grafting and interlayer functionalization for PFOA separation in polyamide membranes, Water Res. X 27 (2025).
[54] M. Koli, et al., Tailoring nanofiltration membranes with MOF 303 modified support layer for enhanced PFAS and heavy metal separation, Desalination 616 (2025).